REVISION 1

# Experiments and models on $H_2O$ retrograde solubility in volcanic systems

**Amy G. Ryan[1]**

**James K. Russell[1], Alexander R.L. Nichols[2], Kai-Uwe Hess[3]**

**and**

**Lucy A. Porritt[1]**

[1]Centre for Experimental Studies of the Lithosphere, Earth, Ocean and Atmospheric Sciences, University of British Columbia, Vancouver, British Columbia, V6T-1Z4, Canada

[2]Research and Development Center for Ocean Drilling Science, Japan Agency for Marine Earth Science and Technology (JAMSTEC), 2-15 Nasushima-cho, Yokosuka, Kanagawa 237-0061, Japan

[3]Department of Earth and Environmental Sciences, Ludwig-Maximilians-Universität, Theresienstrasse 41, 80333 Munich, Germany

**American Mineralogist**

Special Collection: Glasses, Melts, and Fluids, as Tools for Understanding Volcanic Processes and Hazard

Submitted April 30, 2014

Revised and Resubmitted September 3, 2014

*Corresponding Author: Amy Ryan: aryan@eos.ubc.ca

## Abstract

We present a suite of 36 high-temperature (900-1100°C), experiments performed on 10 x 10 mm unjacketed cores of rhyolitic obsidian from Hrafntinnuhryggur, Krafla, Iceland under atmospheric pressure. The obsidian is bubble- and crystal-free with an $H_2O$ content of 0.11(4) wt%. The obsidian cores were heated above the glass transition temperature (*Tg*), held for 0.25-24 hours, then quenched. During each experiment the volume of the samples increased as $H_2O$ vapor-filled bubbles nucleated and expanded. Uniquely, the bubbles did not nucleate on the surface of the core, nor escape, conserving mass during all experiments. Within each isothermal experimental suite, the cores increased in volume with time until they reached a maximum, after which continued heating caused no change in volume (measured by He-pycnometry). We interpret these *T*-*t* conditions as representing thermochemical equilibrium between the melt and exsolved vapor. These experiments are modeled to recover the 1-atmosphere, temperature-dependent solubility of water in the rhyolite melt. Our results define the magnitude of retrograde solubility ($-7.1 \times 10^{-3}$ wt% $H_2O$ per 100°C) and provide estimates of the enthalpy and entropy of the $H_2O$ exsolution reaction ($\Delta H° = 17.8$ kJ mol$^{-1}$, $\Delta S° = 107$ J K$^{-1}$ mol$^{-1}$). We conclude by modeling the implications of retrograde solubility for the glass transition temperatures (*Tg*) of cooling volcanic systems at pressures relevant to volcanic conduits and the Earth's surface. All volcanic systems cool; the effects of retrograde solubility are to allow melts to rehydrate by $H_2O$ dissolution as they cool isobarically, thereby depressing *Tg* and expanding the melt window. Ultimately, the melt is quenched at higher $H_2O$ contents and lower temperatures where the isobaric retrograde solubility curve 'catches' the evolving *Tg*.

**Keywords:** rhyolite, hydrous, $H_2O$-solubility, volcanic, experiment, modeling, glass transition, retrograde

## Introduction

All magmas contain dissolved volatiles that strongly affect the thermodynamic and physical properties of melt and dramatically influence magmatic and volcanic processes (Hess and Dingwell, 1996; Navon et al. 1998; Mysen and Acton 1999; Sparks et al. 1999; Zhang 1999; Gardner et al. 2000; Di Matteo et al. 2004; Zhang et al. 2007; Giordano et al. 2008). Exsolution of a fluid phase, where the dissolved volatile reaches supersaturation, affects the bulk properties of magmas, drives many volcanic eruptions, and controls the duration, magnitude, rate and style of eruption (e.g., effusive vs. explosive) (Webster and Botcharnikov 2011; Watkins et al. 2012). Water ($H_2O$) is the most prevalent, and usually the dominant, volatile species in volcanic systems making the low pressure solubility limits of $H_2O$ in silicic melts particularly relevant to many eruptive and post-eruptive volcanic processes (Sparks et al. 1999; Castro et al. 2005; Robert et al. 2008; Kennedy et al. 2010).

There are a plethora of $H_2O$ solubility studies on melts at pressures >50 MPa (Burnham and Jahns 1962; Silver et al. 1990; Holtz et al. 1995; Dixon et al. 1995; Carroll and Blank 1997; Dingwell et al. 1997; Moore et al. 1998; Yamashita 1999; Holtz et al. 2000; Newman and Lowenstern 2002; Papale et al. 2006; Zhang et al. 2007). There are, however, surprisingly few lower pressure (i.e., $\leq$5 MPa) studies of $H_2O$ solubility in silicate melts (Friedman et al. 1963; McMillan et al. 1986; Silver et al. 1990; Liu et al. 2005). This lack of data has been pointed out by numerous authors, including Zhang (1999), Liu et al. (2005), Robert et al. (2008) and Kennedy et al. (2010), yet the data gap persists. A compilation of all 1-atmosphere, $H_2O$ solubility data is presented in Appendix A and comprises 28 values deriving from three experimental studies. These experiments are particularly important for two reasons. Firstly these pressures correspond to a wide variety of volcanic environments (conduits, domes, ignimbrites, lavas) and thus a range of processes (welding, sealing/permeability collapse and flow dynamics). Secondly, these low pressure solubility

experiments are critical for constraining models of $H_2O$ solubility in silicate melts as a function of temperature, pressure, and composition (Yamashita 1999; Di Matteo et al. 2004; Liu et al. 2005).

Here we present a series of 0.1 MPa, high-temperature (*T*) experiments wherein cores of obsidian are heated isothermally above the glass transition temperature (*Tg*) for controlled amounts of time. These experiments allow progressive bubble nucleation and growth with time until thermochemical and mechanical equilibria between the melt and the exsolved $H_2O$ fluid are reached (Figures 1 and 2). Thus, each series of isothermal experiments illustrates the rates of volatile exsolution (volume change) and, ultimately, defines the solubility of $H_2O$ in the rhyolite melt at atmospheric pressure (Figure 2a). These experiments have been used to create a thermodynamic model for the 0.1 MPa temperature dependence of $H_2O$ solubility (retrograde solubility). Furthermore, we explore the effects of retrograde solubility on *Tg*: resorption of $H_2O$ during cooling depresses *Tg* thereby expanding the 'melt window' in volcanic systems and causing melts to quench at higher $H_2O$ contents and lower temperatures.

## Materials

Our experiments use rhyolitic obsidian from Hrafntinnuhryggur, Krafla, Iceland as described and chemically analyzed by Tuffen and Castro (2009) (Table 1). Their work showed the Hrafntinnuhryggur obsidian sampled from a <0.05 $km^3$ outcrop to have a uniform major element chemical composition independent of a diversity of outcrop textures and colors. They reported, based on synchrotron Fourier transform infrared spectroscopy (FTIR) analysis, that the $H_2O$ contents across the outcropping of Hrafntinnuhryggur obsidian varied from 0.11-0.37 wt%. They argued that the variability in $H_2O$ content was a reflection of differences in post-eruption quench paths (Tuffen and Castro 2009).

All experimental cores for this study derive from a single ~1000 $cm^3$ block of pristine obsidian donated by Hugh Tuffen (pers comm 2008). The starting glass is texturally isotropic and homogeneous except for minor occurrences of cryptic flow-banding, and is essentially bubble- and crystal-free. Table 1 is a comparison of the anhydrous bulk chemical composition of the obsidian block measured by X-ray fluorescence to the electron microprobe (EMP) measured composition of Tuffen and Castro (2009). Independently, we have measured the water content of the obsidian block by FTIR (see below) to be 0.11(4) wt% and adopt this value for our work below (Table 1).

Cylindrical sample cores of obsidian (10 x 10 mm) were drilled, trimmed, and the ends ground to make parallel polished end-surfaces (Figure 1). The cores were then dried at ~150°C for 2 to 24 hours prior to measuring core volume ($V_i$) with precision digital calipers ($\sigma \pm \sim 2x10^{-3}$ $cm^3$) and mass ($m_i$) with a high precision balance ($\sigma \pm \sim 0.006$ mg) (Tables 2). The average density ($\rho_i$) of the starting material, based on 43 cores, was 2.394 g $cm^{-3}$ ($\sigma \pm$ ~0.024 g $cm^{-3}$). The porosity ($\phi_i$) of the initial obsidian cores is below detection.

## Experimental Methods

A total of 36 high-temperature, 1-atmosphere experiments were performed on cores of obsidian in a Nabertherm HTC 08/15 furnace (Figure 2b). Each experiment had a prescribed dwell time ranging from 0.25-24 hours at a constant experimental temperature ($T_{exp}$) varying from 900-1100°C (Figure 2b; Table 2). Our range of $T_{exp}$ is >100°C above the calorimetric glass transition temperature ($Tg$ = 690°C ± 20) of the Hrafntinnuhryggur obsidian as determined by Castro et al. (2008). The obsidian cores were placed in a furnace on a pre-heated ceramic base thereby ensuring that the obsidian cores were heated uniformly (i.e., the ceramic plate did not behave as a heat sink). Two independent K-type thermocouples were used to monitor the internal temperature of the furnace and showed the

125 temperature to be ±5-10°C of its set temperature. Once the prescribed dwell time was reached
126 the ceramic plate and vesiculated obsidian core were removed from the furnace allowing
127 them to quench to below the nominal *Tg* (i.e., 690°C) within 10-15 seconds (measured by
128 thermocouples). There was no change in the geometry of the expanded glass cores during
129 cooling (Figure 1).

130 In order to prevent fracturing of the cores when they were introduced into the furnace
131 we modified our procedure for the high *T* (>1000°C) suites of experiments. Specifically, the
132 cores were introduced into the furnace at lower temperatures and then heated slowly (5-
133 12.5°C $min^{-1}$) to $T_{exp}$. Replicate experiments involving isothermal heating at $T_{exp}$ vs. ramping
134 up to $T_{exp}$ produced cores with equivalent density indicating that the final vesiculation was a
135 product only of $T_{exp}$ and time.

136 We performed two other ancillary experiments. The first tested the influence of
137 sample dimensions and surface roughness on the vesiculation process and vesicle retention.
138 For this experiment (glass 4; Table 2) an angular chip of obsidian featuring smooth
139 conchoidal fracture surfaces was allowed to vesiculate using the same method described
140 above. Replicate *T-t* experiments involving the obsidian chip and 2 sample cores produced
141 products having identical (± 0.01 g $cm^{-3}$) densities. We take this agreement to indicate that
142 the machined surfaces of the cores do not change the bulk behavior of the material by
143 facilitating $H_2O$ escape or enhancing vesiculation.

144 We also ran three reversed experiments at 950°C, 1000°C and 1050°C to test the
145 reproducibility of our results (e.g., AR-IK-34, AR-IK-47 and AR-IK-48). The reversed
146 experiments approached the final vesiculated state from lower and higher temperatures to test
147 that the state is path-independent. Samples were introduced at temperatures below $T_{exp}$, then
148 heated above $T_{exp}$ and allowed to vesiculate for 0.25-1 hours. Presumably at this point the
149 cores exsolved more $H_2O$ due to a decrease in solubility relative to $T_{exp}$. The cores were then

cooled back down at a rate of 2-3°C $min^{-1}$ to $T_{exp}$ and allowed to dwell at $T_{exp}$ for 0.5-2.5 hours. The samples were removed and quenched as described above. The reversed experiments have densities that differ by ≤ 0.1 g $cm^{-3}$ from the 'unreversed' experimental products taken from the equilibrium plateaus at 950°C, 1000°C and 1050°C (Table 2). Thus, the final density of the sample is not greatly influenced by the *T*-path of the experiment, but rather is dependent on $T_{exp}$ and dwell time. This, however, would not be valid for *T*-*t* curves in the growth regime because the slopes of the growth curves are different for different *T*'s, and the total time would be an integrated path of one growth curve plus another (Figure 3).

## Analytical Methods

### Physical properties

For each experimental run product we measured final mass ($m_f$) and volume ($V_f$) (Table 2); volumes of the irregularly shaped swollen cores (Figure 1) were measured with a Micromeritics AccuPyc II 1340 helium pycnometer having an analytical uncertainty ± 0.04%. Masses were measured with a high precision balance (σ ± ~0.006 mg). The final density ($\rho_f$) of the materials was derived from these two measurements. The propagated uncertainties on the calculated values of density, volume change ($\Delta V$), and porosity are ~$6x10^{-4}$ g $cm^{-3}$, 0.02 $cm^3$ and 1.38%, respectively and are corroborated by replicate measurements.

### XCT

We selected a suite of undeformed samples and experimental run products for imaging by X-ray computed tomography (XCT) and for parallel analysis of water contents by FTIR. XCT 3D high-resolution images were acquired using a GE phoenix® v|tome|x s 240 micro-CT scanner at the Institute of Medical Engineering at the Technische Universitat

Munchen (IMETUM) facility, Germany using a high-power X-ray tube and a drx-250 rt detector system. Experimental conditions: 1000 images for 360° (average of 3 single images, one image skipped), exposure time: 333 ms, voltage: 80 kV, current: 130 μA, using a 0.2 mm VA-steel filter.

The resulting set of radiographs was then used to generate a 3D image using the inverse radon transformation (Deans, 2007); the resulting object has a 18.5 μm voxel size. The resulting raw 2D and 3D TIFF images were then processed using ImageJ (Abramoff et al. 2004; Schneider et al. 2012) to optimize contrast in the greyscale images (Figure 1). To isolate bubble populations within the sample for further analysis, the individual datasets were then segmented and analyzed using the Avizo® Fire program (version 8) by the FEI Visualization Sciences Group. These analyses were used to calculate an average bubble radius between all samples (0.322 mm; Appendix C) for subsequent internal pressure calculations (see below).

**FTIR**

Six samples, including the starting glass and glassy run products, were prepared as 100-330 μm-thick wafers and analyzed by FTIR for total water content at the Institute for Research on Earth Evolution (IFREE) at the Japan Agency for Marine Earth Science and Technology (JAMSTEC). Analyses were performed in the mid-IR region over 512 scans at a resolution of 8 $cm^{-1}$ using a heated ceramic (globar) infra-red source, a Ge-coated KBr beamsplitter and a liquid-nitrogen cooled $HgCdTe_2$ (MCT) detector. The wafers were placed on an $H_2O$-free IR-invisible KBr window. Background analyses were taken through the window, before the wafer of glass was positioned in the beam path to measure sample spectra. The results are $H_2O$ contents averaged from eleven to sixteen individual 'spot tests' on the starting material and five experimental products from the 900°C, 950°C, 1000°C,

1050°C and 1100°C temperature suites (AR-IK-24, AR-IK-25, AR-IK-18, AR-IK-23, AR-IK-31) (Table 3). $H_2O$ contents (wt%) were calculated using the height above a linear baseline of the peak at 3550 $cm^{-1}$, a density for rhyolite of 2350 g $l^{-1}$ (Stevenson et al., 1994), a molar absorption coefficient of 90 l $mol^{-1}$ $cm^{-1}$ for rhyolite (Hauri et al., 2002) and thickness estimated from the peak at 1830 $cm^{-1}$ (following Miwa and Toramaru, 2013). Thickness was not measured directly due to the fragility of the experimental products and the difficulty of positioning the measuring needle on the analyzed spot due to the small areas of glass between vesicles.

In addition, 2D micro-distributions in water content were measured in five samples (Figure 4) including the starting material (AR-IK-UND) and four duplicated experimental run products from the 1000°C experimental suite: BF-IK-16, heated for 0.5 hours to a final porosity of 40.7%; BF-IK-2, heated for 1.5 hours to a final porosity of 57.6%; BF-IK-1, heated for 2.5 hours to a final porosity of 62.0%; and BF-IK-3.5, heated for 6 hours to a final porosity of 66.5% (Figure 4). Wafers of these samples were prepared to a thickness of 200-330 μm and color contour FTIR spectroscopic images of the residual $H_2O$ content were collected using the same set up as above and a liquid-nitrogen cooled Focal Plane Array (FPA) MCT detector. The FPA MCT detector produces 350 x 350 μm images each made up of 4096 spectra, giving a resolution of about 5.5 μm. Five to twenty of these images were combined to produce mosaics covering larger areas (von Aulock et al., 2013). $H_2O$ contents (wt%) were calculated from spectra as for the spot tests. Thus images of the 3550 cm-$^{1}$ peak normalized by the 1830 $cm^{-1}$ peak, assuming constant density and molar absorption coefficients (i.e., compositional homogeneity), are proportional to actual $H_2O$ concentration and take into account any change in thickness across a wafer (von Aulock et al., 2014). It cannot be ruled out that the apparent high-$H_2O$ concentration rims around the edge of bubbles

are an artifact of the imaging associated with noise on the image spectra as a result of the bubble edge.

## Results of High T Experiments

Exposure to temperatures above *Tg* (900-1100°C) produces variably expanded bubble-rich run products featuring smooth outer surfaces free of scalloping (Figure 1). The high-*T* experiments cause exsolution of volatiles in the obsidian because the Icelandic glasses were initially quenched with water contents above their 1-atmosphere solubility limits. The extent of exsolution of $H_2O$ fluid at constant *T* is manifest by a change in volume (increased porosity) that depends on the experimental dwell time and on the 1-atmosphere solubility of $H_2O$ at that *T* (Figure 1). The bubbles formed are assumed to be dominantly $H_2O$.

The range in $\Delta V$ is 0.02-1.78 $cm^3$ and is a direct indication of bubble formation and growth (Table 2). Mass changes ($\Delta m$) between the starting core and final cooled experimental product are small but quantifiable (0.19 to 2.26 mg) and are positively correlated to $\Delta V$ (Appendix B). We ascribe the mass loss to the escape of the exsolved $H_2O$ upon quenching as a result of microfracturing in the cores (see Appendix B). The smooth exterior surfaces of the cores and the bubble distributions illustrated by XCT (Figure 1) indicate that the bubbles form and grow during the experiment but fail to perforate the core walls to degas. This fact allows us to treat each experiment as a closed system where the original $H_2O$ is conserved and partitioned between the bubbles and the residual melt. The corollary to this is that all volume change is a direct proxy for the volumetric amount of volatile exsolution at 1-atmosphere and *T* in a fixed amount of time (Figure 3).

### Porosity-time patterns

Each isothermal suite of experiments shows a systematic increase in sample volume, expressed as porosity ($\phi_f$), with increasing dwell time (*t*) until a maximum stable sample

249 volume (e.g., porosity) is attained (Figure 2a, 3). We interpret the initial increase in sample
250 volume (the curvilinear portion in Figure 2a; 3) to be the kinetically controlled bubble
251 nucleation and growth regime and a response to an initial $H_2O$-oversaturation at 1 atm and
252 $T_{exp}$. The plateau in sample volume, denoted by the horizontal portion of the curves (cf. Fig.
253 2a; 3), marks the cessation of exsolution and bubble growth and is due to equilibrium being
254 reached. This fixed maximum porosity is indicative of the $H_2O$ solubility limit for that
255 temperature at 1 atm. In this way we use volume change as an expression of the amount of
256 $H_2O$ that is exsolved from the melt to achieve equilibrium. Thus, porosity is inversely
257 proportional to the equilibrium concentration of $H_2O$ in the glass.

258 The rate of change of sample volume ($v' = dV/dt$) and the time ($\Delta t_e$) to achieve the
259 equilibrium plateau depend on experimental temperature. Specifically, the value of $v'$ and $\Delta t_e$
260 are quantified by the slope and length of tangent lines to the curvilinear portions in Figure 3.
261 At higher temperatures sample volume increases rapidly ($v'$, steep slope) and the plateau is
262 reached in a short amount of time ($\Delta t_e$, e.g., 1-2 hours at 1050°C; Table 2, Figure 3). At lower
263 temperatures the bubble nucleation and growth rates are substantially slower (flatter slope)
264 and it takes longer to reach the equilibrium plateau (e.g., 20-25 hours at 900°C; Table 2,
265 Figure 3).

266 The variations in the porosity-time patterns show the relationship between bubble
267 growth rates and temperature and are reflections of the effect of temperature melt viscosity
268 ($\eta$). More importantly for this research, the final porosity value (i.e. plateau) of the $\phi_f$ - $t$
269 curves increases with experimental temperature, from ~42% at 900°C to ~70% at 1100°C
270 (Table 2, Figure 3). Thus the maximum porosity value is inversely proportional to $T$ and is a
271 qualitative expression of the retrograde solubility of $H_2O$.

272 Some of the longest-term experiments do show signs of partial collapse. For example,
273 in the 925°C suite of experiments (Figure 3b), the core volume is reduced by 10% in the 4

hours of dwell time after reaching the equilibrium solubility limit. This additional time at $T_{exp}$ is enough to allow for some viscous relaxation of the sample, especially given the effect of porosity on the effective viscosity of the core (Quane et al. 2009). A porosity of 50% can cause a 10-fold decrease in the bulk viscosity of the core (from $10^{7.9}$ Pa s for the unvesiculated melt to $10^{7.1}$ Pa s) thus decreasing the relaxation timescale of the vesicular core and facilitating partial collapse. That said, not all cores experience collapse. The 1000°C suite of experiments are stable for 13 hours; 7 hours after reaching the equilibrium plateau the sample shows an apparent porosity decease of less than 2-3%.

**FTIR $H_2O$ images**

FTIR contour images were created for polished wafers cut from cores of starting material and the run products of the 1000°C experiments held at $T_{exp}$ for 0.5, 1.5, 2.5 and 6 hours (Figure 4). A mosaic of $H_2O$ contour images for the starting material shows a weak (<0.01 wt%) variation of $H_2O$ content, creating relatively 'water-rich' and 'water-poor' bands 100-200 μm in width (Figure 4a). Over short experimental dwell times, the banding has a minor influence on bubble nucleation behavior and bubble distribution (Figure 1b,f), however, with increasing dwell time the run products show homogeneous $H_2O$-distributions (Figure 4b,c,d,e). This indicates that over the dwell time of the experiments the dissolved $H_2O$ is readily mobilized to produce a homogeneous distribution of residual $H_2O$.

As stated above, we attribute the high $H_2O$ concentration rims to artifacts related to the imaging process. To verify this assumption we have assessed the potential for diffusion-limited resorption of $H_2O$ from the bubbles to the melt during the quenching of the samples. The relationship between diffusion coefficients ($D$), time ($t$) and diffusion length scale ($L_D$) ($L_D = (4*D*t)^{0.5}$) suggests trivial (5-10 μm if $t$ = 15 s) effective diffusion length scales and thus an insignificant amount of rehydration.

FTIR spot analyses of the starting material and experimental products at equilibrium at 900°C, 950°C, 1000°C, 1050°C and 1100°C quantify the equilibrium concentration of $H_2O$ in the rhyolitic glass at 1 atm for these temperatures. These measurements show a change in the $H_2O$ content of the residual glass with increasing $T_{exp}$ from an initial 0.114 wt% (s.d. 0.013) to 0.098 wt% (s.d. 0.010), 0.087 wt% (s.d. 0.009), 0.093 wt% (s.d. 0.008), 0.090 wt% (s.d. 0.006) and 0.108 wt% (s.d. 0.010) for 900°C, 950°C, 1000°C, 1050°C and 1100°C respectively (Table 3).

The mosaics of 2D FTIR contour images are most useful for demonstrating the homogeneous distributions of $H_2O$ in the run products. Unfortunately, the individual spot analyses are not precise enough to quantify the changes in $H_2O$ contents. The lack of precision is at least partly due to the complexity of measuring highly vesicular samples.

**Calculated $H_2O$ contents in glasses**

In our analysis of the experimental data we assume that volume expansion of the sample results only from bubble formation and expansion and that thermal expansion of the melt (potentially captured during quenching) can be neglected. This assumption is justified because the maximum volume change predicted for the melt being heated to 1100°C is 0.65% (Bagdassarov and Dingwell, 1992), which is within our measurement uncertainties for porosity (1.38%). Similarly, we ignore the potential slight variations in glass density caused by different quench rates (nature vs. experiment; Vollmayr et al. 1996). Here, we use the volume change ($\Delta V$; Figure 5a) to compute the total $H_2O$ exsolved from the melt at the experimental conditions by determining the internal pressure of the bubbles ($P_i$) and using the Redlich-Kwong equation of state to calculate the $H_2O$ vapor content in the bubble fraction. We then compute the $H_2O$ content of the residual melt by difference, thereby establishing the

1-atmosphere solubility of $H_2O$ in the rhyolite melt, and the *T*-dependence of the $H_2O$ solubility at 1-atmosphere.

We compute the internal pressure of the bubbles using a modified form of the Rayleigh-Plesset equation:

$$P_i - P_e = \rho_m \left( r \frac{d^2 r}{dt^2} + \frac{3}{2} \left( \frac{dr}{dt} \right)^2 \right) + \frac{4\eta}{r} \frac{dr}{dt} + \frac{2\sigma}{r} \qquad \text{(Eq. 1)}$$

where $P_i$ is the pressure within the bubble (Pa), $P_e$ is the external pressure of the system (Pa), $\rho_m$ is the density of the melt (kg $m^{-3}$), *r* is bubble radius (m), *t* is time (s), η is melt viscosity (Pa s) and σ is the surface tension of the melt (N $m^{-1}$) (e.g., Sparks 1978; Barclay et al. 1995; Toramaru 1995; Navon et al. 1998; Liu and Zhang 2000; Blower et al. 2001; Proussevitch and Sahagian 2005). Some terms in Eq. 1 can be considered negligible under specific conditions and eliminated. For the purposes of our calculations, we eliminate the terms for inertial and viscous forces based on the following:

i) our experiments are isobaric and static, thus, $P_e$ is a constant $10^5$ Pa and inertial forces (1st term) are negligible;

ii) viscous forces form an important resistance during bubble growth (Proussevitch and Sahagian, 1998) but as the bubbles achieve their final equilibrium state viscous forces become irrelevant and can be ignored (2nd term).

There are two situations where the surface tension term (3rd term; Eq. 1) dominates in the calculation of internal pressure. The first is where bubbles are small and near the critical radius for spontaneous growth (e.g., $<10^{-3}$ cm (Sparks 1978)) (Sparks 1978; Prousevitch et al. 1993; Barclay et al. 1995; Toramaru 1995; Liu and Zhang 2000). The second case is where bubbles are no longer growing and have achieved their equilibrium size (Toramaru 1989, 1995). Given the negligible effects of inertial and viscous forces on the final distribution of bubbles (e.g., on the equilibrium plateau) we calculate internal pressure from:

$$P_i = P_e + \frac{2\sigma}{r} \qquad \text{(Eq. 2)}$$

Surface tension (σ) acts as a force that opposes an increase in the surface area of a phase and, here, exists between the silicate melt and the supercritical fluid produced by exsolution of dissolved $H_2O$. A recent review of surface tension data by Gardner and Ketcham (2011) has shown a small *T*-dependence for melt-fluid σ ($9x10^{-5}$ N $m^{-1}$ $°C^{-1}$). A compilation of all published σ values for hydrous (3.5-9.3 wt% $H_2O$) compositions from basaltic andesite to rhyolite to phonolite also fell within the narrow range of 0.042-0.110 N $m^{-1}$ (Mourtada-Bonnefoi and Laporte 1999, 2002, 2004; Bagdassarov et al. 2000; Mangan and Sisson 2000, 2005; Gardner and Ketcham 2011; Gardner 2012; Gardner et al. 2013). Conversely values for σ increase dramatically from hydrous (0.042-0.110 N $m^{-1}$) to anhydrous silicate melts (0.282-0.371 N $m^{-1}$) (Walker and Mullins 1981; Bagdassarov et al. 2000). Water appears to be more important than melt composition and temperature, therefore, in lieu of published data at low water contents (i.e., <1 wt%) we used the average value for all hydrous data (0.081 N $m^{-1}$). For this surface tension value, the calculated internal pressure of bubbles ($P_i$) is 101828 Pa (Table 3) for an average bubble radius ($r$) of 0.322 mm (from XCT imaging; Figure 1; Appendix C). The error in $P_i$ associated with the selection of values for σ and $r$ is small: a 3-fold increase or decrease in $r$ cause ~1% change in $P_i$. Similarly using an anhydrous surface tension value of 0.3 N/m increases $P_i$ by ~1.5%.

Using this $P_i$ value, the initial number of moles of $H_2O$ in the glass of each sample ($n_i$) (Table 3), the change in sample volume ($\Delta V$; Figure 5a) and the Redlich-Kwong equation of state we calculate the moles of $H_2O$ vapor in the bubbles formed during each experiment ($n_b$) using the following equation:

$$\frac{2\sigma}{r} + P_e = \frac{R\,T}{\frac{\Delta V}{n_b} - b} - \frac{a}{\sqrt{T}\,\frac{\Delta V}{n_b}\left(\frac{\Delta V}{n_b} + b\right)} \qquad \text{(Eq. 3)}$$

where $a$ and $b$ are constants that correct for the attractive potential of molecules and for volume, respectively (Redlich and Kwong 1949), R is the universal gas constant and $T$ is temperature in Kelvin (Table 3). Solving for $n_b$ we compute the number of moles of $H_2O$ in

the residual glass ($n_r$) by subtracting $n_b$ from the number of moles of $H_2O$ in the core at the start of the experiment ($n_i$) and then convert to a value of wt% $H_2O$ in the residual glass (Table 3). The calculated residual water contents of the glass mirror the relative change in sample volume with time and temperature (Figure 5). Minimum $H_2O$ values in each temperature suite correspond to data that lie on the equilibrium plateau and decrease with increasing temperature.

## Discussion

### Retrograde solubility: comparison to published models

Figure 6a plots ln $x_{H2O}$ against reciprocal temperature for all experimental suites as well as a linear model fitted to the data points that define our equilibrium plateaus (solid symbols) from 900-1050°C (Figure 3a,b,c,d,e):

$$\ln x_{H2O} = 1069.6/T - 6.4637 \qquad \text{(Eq. 4)}$$

where $x_{H2O}$ is the mole fraction of water in the glass and $T$ is the experimental temperature (K). We have chosen to remove the 1100°C data point, which does not fall on the well-defined linear trend. At 1100°C the time to equilibrium ($\Delta t_e$) competes with the viscous relaxation timescale, effectively meaning the 1100°C is at the limit of the experimental-window using this methodology. Even though the experimental $t$-window is small (2 hours; Figure 3f) we suspect that we failed to capture the maximum volume expansion of the plateau sample at this temperature.

Figure 6b shows our data and model against all published 0.1 MPa $H_2O$ solubility data (Table A1) and the models produced by Newman and Lowenstern (2002), Liu et al. (2005) and Zhang et al. (2007). Our data extend from 900-1100°C and are consistent with the experimental data of Liu et al. (2005) over the same temperature range and down to 700°C. In addition, our model, which estimates the magnitude of the 0.1 MPa of retrograde solubility

398 at ~ -7.1x10$^{-3}$ wt% $H_2O$ per 100°C from 700-1200°C (Figure 6b), fits not only our data, but
399 when extrapolated to temperatures below 700°C, also captures some of the data produced by
400 Liu et al. (2005). Our estimates of the magnitude of retrograde solubility agree well with
401 those predicted by the models of Zhang et al. (2007) and Liu et al. (2005) (~ -7.8 x 10$^{-3}$ wt%
402 $H_2O$ per 100°C and ~ -13.9 x 10$^{-3}$ wt% $H_2O$ per 100°C, respectively; Figure 6b). However,
403 the Zhang et al. (2007) model fails to capture both our data and the low pressure date of Liu
404 et al. (2005). The Newman and Lowenstern (2002) model agrees well with our data despite
405 being constrained by almost no experimental data at 0.1 MPa. On this basis, we are confident
406 that our data and model accurately capture the 0.1 MPa retrograde solubility within our
407 experimental window (900-1100°C) and at lower temperatures (i.e., 700-900°C). The
408 consistency in the data and the calculated values of retrograde solubility shown between the
409 Liu et al. (2005) model and our results suggests that the Liu et al. (2005) model is the best of
410 the multi-pressure models for (at least) low pressure situations.

411 Based on the empirical fit shown as Eq. 4 we have calculated the implied standard
412 state enthalpy and entropy values for the exsolution of $H_2O$ from the melt: $\Delta H°$ = 17.8 kJ
413 mol$^{-1}$; $\Delta S°$ = 107 J K$^{-1}$ mol$^{-1}$ (see Appendix D). The positive value of $\Delta H°$ shows that this
414 reaction is endothermic, allowing for slight decreases in system temperature with
415 vesiculation. Liu et al. (2005) derived similar exsolution enthalpy values (13.2-16.5 kJ mol$^{-1}$
416 at 0.1-11 MPa) and concluded that exsolution does not have a significant effect on the
417 temperature of the rhyolitic melt.

418

419 **Retrograde solubility: The effect on *Tg***

420 Below, we have explored the wider implications of retrograde solubility for volcanic
421 processes. Figure 7 shows the calculated isobaric solubility curves for a rhyolite melt over a
422 range of pressures (0.1-40 MPa) as modeled by Liu et al. (2005). At constant temperature,

423 $H_2O$ solubility is strongly controlled by and increases with pressure. Additionally, each
424 isobaric curve shows the increase in the solubility of water with decreasing temperature
425 (1000-400°C). At atmospheric pressure the effect is slight, as evidenced by the near vertical
426 slope of the isobaric curve from both models. However, at higher pressures the slopes of the
427 isobaric curves become increasingly negative. Ultimately the change in the negative slopes of
428 the $T$-$X_{H2O}$ curves maps out the change in the magnitude of retrograde solubility with
429 pressure. This shows that, as volcanic systems cool, the capacity for $H_2O$ dissolution in melts
430 increases substantially with increasing pressure, allowing for increasing melt rehydration.
431 Figure 7 also shows values of *Tg* calculated for the Hrafntinnuhryggur rhyolitic melt
432 as a function of water content using the viscosity (η) model of Giordano et al. (2008) (*Tg* ~ *T*
433 where $\eta = 10^{12}$ Pa s). The addition of water to anhydrous melts causes a strong initial
434 reduction in *Tg* but at higher water contents the rate of decrease in *Tg* lessens (Hess and
435 Dingwell, 1996). The calculated glass transition curve cuts across the pressure dependent
436 water solubility curves at a high angle to create a series of [$T$-$X_{H20}$] intersection points. These
437 intersections mark the termination of isobaric $H_2O$ solubility curves for volcanic systems. As
438 the melt cools moving down the isobaric solubility curves, it redissolves magmatic volatiles,
439 causing the *Tg* of the hydrated melt to decrease continuously, thereby, expanding the melt
440 (vs. glass) window. This effect of $H_2O$ content on *Tg* creates a positive feedback loop, or
441 'chase scenario' where the decreasing *T* of the system chases the falling *Tg* (Figure 8 inset).
442 Ultimately, however, the decrease in *Tg* with increasing water content (i.e., slope of *Tg*
443 curve) is insufficient to avoid intersection with the steep isobaric retrograde solubility curves
444 at volcanic to subvolcanic temperatures. Thus, during cooling the isobaric retrograde
445 solubility curve intersects the $H_2O$-dependent *Tg* curve and the melt is quenched to a glass
446 (i.e., 'rehydration quench'; Figure 8 inset).

At this point the $H_2O$ content is 'frozen in' corresponding to the $T$-$P$-$X_{H2O}$ coordinate of the intersection; below the *Tg* curve the predicted isobaric $H_2O$ solubility curves become metastable extensions (dashed lines; Figure 7). The values defined by the intersection of the solubility and *Tg* curves are maximum $H_2O$ contents for dissolution of $H_2O$ fluid (solute) into the silicate melt (solvent). This is because the melt solubility curves are for a solvent ($T_{melt}$ > *Tg*) having a specific set of thermochemical and structural properties distinct from the corresponding glass (<*Tg*).

The *Tg* limitation on water solubility in silicate melt is, however, not relevant to secondary, non-magmatic (re)hydration processes that operate at temperatures below *Tg* (e.g., devitrification, perlitization, palagonitization), where glasses with substantially higher water contents can be created (i.e., Anovitz et al. 2008). This lower temperature rehydration of silicate glass is demonstrated serendipitously by the 550°C experiments of Liu et al. (2005) which resulted in anomalously high, but reproducible, $H_2O$ contents. Liu et al. (2005) recognized these values as a 550°C 'solubility' limit but, because the experiments were below the glass transition curve, did not include these data in their $H_2O$ solubility (melt) model. The mechanisms for hydration of volcanic glasses below *Tg* are incompletely understood but must be the result of alternative means of water dissolution (Anovitz et al. 2008; Giachetti and Gonnermann 2013).

## Implications for volcanic processes

The glass transition is an important limiting value for the temperature conditions at which many volcanic processes take place. Above *Tg*, rates of nucleation, crystallization and vesiculation are fast enough to significantly affect magmatic processes. Conversely, where the $T$-$X_{melt}$ path of the melt intersects the *Tg* of the melt, glass forms and many magmatic and volcanic processes effectively cease.

There are a variety of ways in which volcanic systems approach and intersect their glass transition (Fig. 8; inset). Conventionally, volcanic systems can be cooled at rates faster than they can vesiculate and crystallize to the point that the isochemical melt reaches its *Tg* to form glass (thermal quench). All volcanic systems exsolve gas as they rise to the Earth's surface and the associated loss of $H_2O$ from the melt due to degassing can cause a rapid and substantial rise in the *Tg* of the melt thereby reducing the melt window (Fig. 8, inset). Where the degassing-induced rise in *Tg* intersects the melt temperature ($Tg = T_{melt}$) the melt transitions to glass (degassing quench). The retrograde solubility of $H_2O$ provides a means of expanding the melt field relative to the glassy state. In a wide range of volcanic systems where cooling timescales are slow enough to facilitate $H_2O$ diffusion in silicate melts, the melts have the opportunity to resorb $H_2O$ as they cool. The consequence of this is to reduce the effective *Tg* of the melt allowing for further uptake of $H_2O$ with cooling. Ultimately, however, the reduction in *Tg* with increasing $H_2O$ content is insufficient to avoid intersecting the isobaric solubility curve where a rehydration quench of the **melt** occurs.

Figure 8 shows several potential cooling paths in a schematic volcanic system and their effect on the final $H_2O$ content of the quenched melt, including: i) conventional thermal quenching (A), and ii) slower cooling along the retrograde solubility curve until the glass transition temperature curve is intersected (i.e., rehydration quench; $B_1$, $B_2$ and $B_3$). The differences in the final $H_2O$ content and *Tg* of the melt arising from thermal vs. rehydration quenching increase substantially with increasing pressure.

Retrograde solubility mainly plays a role in volcanic systems where cooling is slow enough to support vapor-melt equilibrium. For rehydration to occur the system must also contain $H_2O$-rich fluids available for resorption. Highly efficient degassing of volcanic systems (Sparks et al. 1999) would favor a degassing quench over rehydration quenching. We have identified three volcanic environments where the retrograde solubility of $H_2O$ can play

497 an important role, including: welding of pyroclastic deposits, flow of silicic lavas, and the
498 forensic recovery of fragmentation depths.

499 Recent studies of welding processes and timescales have emphasized the role $H_2O$
500 plays in inducing or prolonging welding (Friedman 1963; Sparks et al. 1999; Giordano et al.
501 2005; Grunder and Russell 2005; Keating 2005; Robert et al. 2008; Kolzenburg and Russell,
502 2014). Sparks et al. (1999) discussed the role of load *P* in causing rehydration of vitric
503 juvenile pyroclasts in ignimbrite sheets. The rehydration causes a concomitant viscosity
504 reduction and, thus, facilitates welding. The 'gas retention regime' of their conceptual model
505 requires pore fluid pressure to equal load pressure, implying very low permeability or
506 extremely rapid compaction. Their isothermal conceptual model did not consider an
507 alternative explanation involving the effects of retrograde solubility, which has a marked
508 effect even at low pressures (i.e., < 20 MPa; Figure 9a). In a 100 m thick ignimbrite sheet for
509 example (e.g., Fish Canyon Tuff, Rio Caliente, Cerro Galan, Bishop Tuff (Cas and Wright,
510 1988)) discounting the effects of retrograde solubility leads to an underestimation of the final
511 $H_2O$ content of a melt by 0.1 wt% at 2 MPa, assuming an isothermal system at 800°C (Figure
512 9b). Because there is a concordant decrease in *Tg* with increasing $H_2O$, assuming an
513 isothermal body also overestimates the effective viscosity of the material. For example, in a
514 model for an ignimbrite (i.e., 2 MPa) that considers rehydration along the cooling path rather
515 than an isothermal (800°C) system, *Tg* decreases by ~15°C, thereby expanding the melt
516 window and prolonging welding (Figure 9b). Figure 9c is an extension of these same curves
517 to conduit-relevant depths of 2 km. At these pressures (up to 40 MPa), the difference between
518 the $H_2O$ content and *Tg* of an isothermal and a cooling system is 1 wt% $H_2O$ and ~75°C,
519 respectively. At 40 MPa the *Tg* of the melt on the retrograde solubility path is nearly half the
520 value of the corresponding anhydrous glass transition of the melt. This remarkable decrease
521 in *Tg* will dramatically change the timescales available for welding of materials filling the

522 volcanic conduit (Russell and Quane, 2005; Kolzenburg and Russell, 2014). Although the
523 overall effect of retrograde solubility is small relative to the *P*-dependence of $H_2O$ solubility,
524 it increases the melt window in a cooling pyroclastic body substantially and will greatly
525 facilitate welding.

526 Similarly, *P*- and *T*-dependent $H_2O$ concentrations may play an important role in
527 explaining the transport and cooling timescales of rhyolitic lava flows. Two primary models
528 have been proposed to explain the eruption and emplacement of these dense (i.e., low
529 porosity), high viscosity melts: extensive degassing in the conduit prior to eruption (Jaupart
530 and Allegre 1991; Gonnermann and Manga 2003; Yoshimura and Nakamura 2008; Castro et
531 al. 2012) vs. initial extrusion of an inflated magmatic foam that subsequently collapses to
532 form a dense lava (Eichelberger et al. 1986; Westrich et al. 1988; Westrich and Eichelberger
533 1994). Several mechanisms have also been invoked to explain the lateral extent of these high-
534 viscosity magmas: extremely efficient heat retention (Manley, 1992; Tuffen et al. 2013) vs.
535 changes in magma rheology related to the presence and distribution of bubbles (Eichelberger
536 et al. 1986; Castro and Cashman, 1999; Vona et al. 2013). Retrograde solubility could also
537 explain some of the enigmatic behavior and textures found in rhyolite flows. Once erupted on
538 the surface, whether as a relatively dense or foamed body, rhyolite will begin to cool and
539 resorb $H_2O$ as dictated by *P* (i.e., flow thickness) and *T* (eruption temperature and cooling
540 history) conditions (Figure 9a). This resorption process, which could possibly eradicate
541 foamed textures (Westrich and Eichelberger 1994), would lead to a decrease in viscosity, as
542 well as depression in *Tg*, prolonging the life of a flowing viscous body (Figure 9b). Coupled
543 with thermal efficiency and the effect of bubbles on magma rheology, retrograde solubility
544 could explain the impressive lateral extent of some rhyolite lava flows.

545 Forensic investigations of storage and fragmentation depths and eruption dynamics
546 are commonly based on measured $H_2O$ contents in melt inclusions or glasses to estimate

pressure (Atlas et al. 2006; Rust and Cashman 2007; Wright et al. 2007). $H_2O$ contents coupled with $H_2O$ distribution and textural data have also been used to identify specific pressure cycling events, such as at Mono Craters, California (Watkins et al. 2012). These studies could be further constrained by considering the *T*-dependence of $H_2O$ solubility as noted by McIntosh et al. (2014). As in welding studies, many forensic volcanology studies have assumed isothermal conditions (Rust and Cashman 2007; Wright et al. 2007) constrained by geothermometry (Rust and Cashman 2007; Watkins et al. 2012). Strong thermal quenching is necessary in each instance to ensure that the isothermal pressure estimates from $H_2O$ contents are valid. However, as many of these volcanic centers are dynamic and complex, there is always the possibility of re-equilibration at different *P*-*T* conditions than those recorded elsewhere in a sample. At the very least, $H_2O$-*P* curves that include considerations of retrograde solubility can provide lower and upper bounds on estimated fragmentation depths (Figure 9c).

## Implications

This high temperature experimental study produced new data on the solubility of $H_2O$ in silicate melts under conditions where the published data are sparse (i.e., 0.1 MPa). These data are used to create a simple thermodynamic model for $H_2O$ solubility from 700-1200°C at 0.1 MPa and the enthalpy and entropy of exsolution of $H_2O$. The data and model corroborates the low-pressure data and model for $H_2O$ solubility of Liu et al. (2005).

The results of this study also highlight the importance of retrograde solubility in volcanology. Pressure changes in volcanic systems lead to dramatic changes in water solubility, especially during ascent, and ultimately control eruption processes. However, volcanic systems generally move from high to low temperature and the inverse relationship between temperature and water solubility plays a critical role in many post-eruption

processes. Our work shows that the effects of retrograde solubility and the potential for rehydration quenching should be considered when interpreting volcanic processes recorded by surficial deposits or within volcanic conduits and feeders.

## Acknowledgements

The NSERC Discovery and Discovery Accelerator Supplements programs and the German Academic Exchange Service funded this work via grants held by JKR. The senior author acknowledges scholarship and travel funding from AmeriCorps, the Mineralogical Association of Canada and the University of British Columbia. We are indebted to Hugh Tuffen (Lancaster University, UK) who generously donated to us a block of obsidian from Hrafntinnuhryggur, Krafla, Iceland, and to Andre Phillion (University of British Columbia Okanagan, BC, Canada) for access to the floating license for Avizo® Fire. We would like to thank Felix von Aulock and an anonymous reviewer for the thorough and constructive reviews, which significantly improved this manuscript.

## References

Abramoff, M.D., Magalhaes, P.J., and Ram, S.J. (2004) Image Processing with ImageJ. Biophotonics International, 11, 36-42.

Anovitz, L.M., Cole, D.R., and Fayek, M. (2008) Mechanisms of rhyolitic glass hydration below the glass transition. American Mineralogist, 93, 1166-1178.

Atlas, Z.D., Dixon, J.E., Sen, G., Finny, M., and Martin-Del Pozzo, A.L. (2006) Melt inclusions from Volcán Popocatépetl and Volcán de Colima, Mexico: Melt evolution due to vapor-saturated crystallization during ascent. Journal of Volcanology and Geothermal Research, 153, 221–240.

von Aulock, F., Nichols, A.R.L., Kennedy, B.M., and Oze, C., 2013. Timescales of texture development in a cooling lava dome. Geochimica et Cosmochimica Acta, 114, 72-80.

von Aulock, F.W., Kennedy, B.M., Schipper, C.I., Castro, J.M., Martin, D. E., Oze, C., Watkins, J.M., Wallace, P.J., Puskar, L., Bégué, F., Nichols, A.R.L., and Tuffen, H., 2014. Advances in Fourier transform infrared spectroscopy of natural glasses: From sample preparation to data analysis. Lithos, 206-207, 52-64, doi: 10.1016/j.lithos.2014.07.017.

Bagdassarov, N.S., and Dingwell, D.B. (1992) A rheological investigation of vesicular rhyolite. Journal of Volcanology and Geothermal Research, 50, 307–322.

Bagdassarov, N., Dorfman, A., and Dingwell, D.B. (2000) Effect of alkalis, phosphorus, and water on the surface tension of haplogranite melt. American Mineralogist, 85, 33–40.

Baker, D.R., Mancini, L., Polacci, M., Higgins, M.D., Gualda, G.A.R., Hill, R.J., and Rivers, M.L. (2012) An introduction to the application of X-ray microtomography to the three-dimensional study of igneous rocks. Lithos, 148, 262–276.

Barclay, J., Riley, D.S., and Sparks, R.S.J. (1995) Analytical models for bubble growth during decompression of high viscosity magmas. Bulletin of Volcanology, 57, 422–431.

Blower, J.D., Mader, H.M., and Wilson, S.D.R. (2001) Coupling of viscous and diffusive controls on bubble growth during explosive volcanic eruptions. Earth and Planetary Science Letters, 193, 47–56.

Burnham, C.W. (1994) Development of the Burnham model for predication of $H_2O$ solubility in magmas. Reviews in Mineralogy, 30, 123-129.

Burnham, C.W., and Jahns, R.H. (1962) A Method for Determining the Solubility of Water in Silicate Melts. American Journal of Science, 260, 721–745.

Carlson, W.D. (2006) Three-dimensional imaging of earth and planetary materials. Earth and Planetary Science Letters, 249, 133-147.

Carroll, M.R., and Blank, J.G. (1997) The solubility of $H_2O$ in phonolitic melts. American Mineralogist, 82, 549–556.

623 Cas, R.A.F., and Wright, J.V. (1987) Volcanic Successions; Modern and Ancient, 528 p.
624 Chapman and Hall, London.
625 Castro, J., and Cashman, K.V. (1999) Constraints on rheology of obsidian lavas based on
626 mesoscopic folds. Journal of Structural Geology, 21, 807-819.
627 Castro, J.M., Manga, M., and Martin, M.C. (2005) Vesiculation rates of obsidian domes
628 inferred from $H_2O$ concentration profiles. Geophysical Research Letters, 32, L21307.
629 Castro, J.M., Beck, P., Tuffen, H., Nichols, A.R.L., Dingwell, D.B., and Martin, M.C. (2008)
630 Timescales of spherulite crystallization in obsidian inferred from water concentration
631 profiles. American Mineralogist, 93, 1816–1822.
632 Castro, J.M., Cordonnier, B., Tuffen, H., Tobin, M.J., Puskar, L., Martin, M.C., and Bechtel,
633 H.A. (2012) The role of melt-fracture degassing in defusing explosive rhyolite eruptions
634 at volcan Chaiten. Earth and Planetary Science Letters, 333-334, 63–69.
635 Deans, S.R. (2007) The radon transform and some of its applications, 295 p. Dover
636 Publishing Company, New York.
637 Di Matteo, V., Carroll, M.R., Behrens, H., Vetere, F., and Brooker, R.A. (2004) Water
638 solubility in trachytic melts. Chemical Geology, 213, 187–196.
639 Dingwell, D.B., Holtz, F., and Behrens, H. (1997) The solubility of $H_2O$ in peralkaline and
640 peraluminous granitic melts. American Mineralogist, 82, 434–437.
641 Dixon, J.E., Stolper, E.M., and Holloway, J.R. (1995) An Experimental Study of Water and
642 Carbon Dioxide Solubilities in Mid-Ocean Ridge Basaltic Liquids. Part I: Calibration and
643 Solubility Models. Journal of Petrology, 36, 1607–1631.
644 Eichelberger, J.C., Carrigan, C.R., Westrich, H.R., and Price, R.H. (1986) Non-explosive
645 silicic volcanism. Nature, 323, 598-602.
646 Friedman, I., Long, W., and Smith, R.L. (1963) Viscosity and Water Content of Rhyolite
647 Glass. Journal of Geophysical Research, 68, 6523–6535.

Gardner, J.E. (2012) Surface tension and bubble nucleation in phonolite magmas. Geochimica et Cosmochimica Acta, 76, 93–102.

Gardner, J.E., and Ketcham, R.A. (2011) Bubble nucleation in rhyolite and dacite melts: temperature dependence of surface tension. Contributions to Mineralogy and Petrology, 162, 929–943.

Gardner, J.E., Hilton, M., and Carroll, M.R. (2000) Bubble growth in highly viscous silicate melts during continuous decompression from high pressure. Geochimica et Cosmochimica Acta, 64, 1473–1483.

Gardner, J.E., Ketcham, R.A., and Moore, G. (2013) Surface tension of hydrous silicate melts: Constraints on the impact of melt composition. Journal of Volcanology and Geothermal Research, 267, 68–74.

Giachetti, T., and Gonnermann, H.M. (2013) Water in volcanic pyroclast: Rehydration or incomplete degassing? Earth and Planetary Science Letters, 369-370, 317–332.

Giordano, D., Nichols, A.R.L., and Dingwell, D.B. (2005) Glass transition temperatures of natural hydrous melts: a relationship with shear viscosity and implications for the welding process. Journal of Volcanology and Geothermal Research, 142, 105–118.

Giordano, D., Russell, J.K., and Dingwell, D.B. (2008) Viscosity of magmatic liquids: A model. Earth and Planetary Science Letters, 271, 123–134.

Gonnermann, H.M., and Manga, M. (2003) Explosive volcanism may not be an inevitable consequence of magma fragmentation. Nature, 426, 432-435.

Grunder, A., and Russell, J.K. (2005) Welding processes in volcanology: insights from field, experimental, and modeling studies. Journal of Volcanology and Geothermal Research, 142, 1–9.

671 Hauri, E., Wang, J., Dixon, J.E., King, P.L. Mandeville, C., and Newman, S. (2002) SIMS
672 analysis of volatiles in silicate glasses 1. Calibration, matrix effects and comparisons
673 with FTIR. Chemical Geology, 183, 99-114.
674 Hess, K.-U., and Dingwell, D.B. (1996) Viscosities of hydrous leucogranitic melts: A non-
675 Arrhenian model. American Mineralogist, 81, 1297-1300.
676 Holtz, F., Behrens, H., Dingwell, D.B., and Johannes, W. (1995) $H_2O$ solubility in
677 haplogranitic melts: Compositional, pressure and temperature dependence. American
678 Mineralogist, 80, 94–108.
679 Holtz, F., Roux, J., Behrens, H., and Pichavant, M. (2000) Water solubility in silica and
680 quartzofeldspathic melts. American Mineralogist, 85, 682–686.
681 Ihinger, P.D., Zhang, Y., and Stolper, E.M. (1999) The speciation of dissolved water in
682 rhyolitic melt. Geochimica et Cosmochimica Acta, 63, 3567-3578.
683 Jaupart, C., and Allegre, C.J. (1991) Gas content, eruption rate and instabilities of eruption
684 regime in silicic volcanoes. Earth and Planetary Science Letters, 102, 413–429.
685 Kennedy, B.M., Jellinek, A.M., Russell, J.K., Nichols, A.R.L., and Vigouroux, N. (2010)
686 Time-and temperature-dependent conduit wall porosity: A key control on degassing and
687 explosivity at Tarawera volcano, New Zealand. Earth and Planetary Science Letters, 299,
688 126–137.
689 Keating, G.N. (2005) The role of water in cooling ignimbrites. Journal of Volcanology and
690 Geothermal Research, 142, 145–171.
691 Kolzenburg, S., and Russell, J.K. (2014) Welding of pyroclastic conduit infill: A mechanism
692 for cyclical explosive eruptions. in press in Solid Earth.
693 Liu, Y., and Zhang, Y. (2000) Bubble growth in rhyolitic melt. Earth and Planetary Science
694 Letters, 181, 251–264.
695 Liu, Y., Zhang, Y., and Behrens, H. (2005) Solubility of $H_2O$ in rhyolitic melts at low

pressures and a new empirical model for mixed $H_2O$-$CO_2$ solubility in rhyolitic melts. Journal of Volcanology and Geothermal Research, 143, 219–235.

McIntosh, I.M., Llewellin, E.W., Humphreys, M.C.S., Nichols, A.R.L., Burgisser, A., and Schipper, C.I. (2014) Distribution of dissolved water in magmatic glass records growth and resorption of bubbles. Earth and Planetary Science Letters, 401, 1-11.

McMillan, P., Peraudeau, G., Holloway, J., and Coutures, J.-P. (1986) Water solubility in a calcium aluminosilicate melt. Contributions to Mineralogy and Petrology, 94, 178–182.

Mangan, M., and Sisson, T. (2000) Delayed, disequilibrium degassing in rhyolite magma: decompression experiments and implications for explosive volcanism. Earth and Planetary Science Letters, 183, 441–455.

Mangan, M., and Sisson, T. (2005) Evolution of melt-vapor surface tension in silicic volcanic systems: Experiments with hydrous melts. Journal of Geophysical Research, 110, B01202.

Manley, C.R. (1992) Extended cooling viscous flow of large, hot rhyolite lavas: implications of numerical modeling results. Journal of Volcanology and Geothermal Research, 53, 27-46.

Miwa, T., and Toramaru, A. (2013) Conduit process in vulcanian eruptions at Sakurajima volcano, Japan: Inference from comparison of volcanic ash with pressure wave and seismic data. Bulletin of Volcanology, 75, 685.

Moore, G., Vennemann, T., and Carmichael, I.S.E. (1998) An empirical model for the solubility of $H_2O$ in magmas in 3 kilobars. American Mineralogist, 83, 36–42.

Mourtada-Bonnefoi, C.C., and Laporte, D. (1999) Experimental study of homogenous bubble nucleation in rhyolitic magmas. Geophysical Research Letters, 26, 3505–3508.

Mourtada-Bonnefoi, C.C., and Laporte, D. (2002) Homogeneous bubble nucleation in rhyolitic magmas: An experimental study of the effect of $H_2O$ and $CO_2$. Journal of

721 Geophysical Research, 107, B4, 2066.
722 Mourtada-Bonnefoi, C.C., and Laporte, D. (2004) Kinetics of bubble nucleation in a rhyolitic
723 melt: an experimental study of the effect of ascent rate. Earth and Planetary Science
724 Letters, 218, 521–537.
725 Mysen, B.O., and Acton, M. (1999) Water in $H_2O$-saturated magma-fluid systems: Solubility
726 behavior in $K_2O$-$Al_2O_3$-$SiO_2$-$H_2O$ to 2.0 GPa and 1300°C. Geochimica et Cosmochimica
727 Acta, 63, 3799–3815.
728 Navon, O., Chekhmir, A., and Lyakhovsky, V. (1998) Bubble growth in highly viscous
729 melts: theory, experiments, and autoexplosivity of dome lavas. Earth and Planetary
730 Science Letters, 160, 763–776.
731 Newman, S., and Lowenstern, J.B. (2002) VOLATILECALC: a silicate melt-$H_2O$-$CO_2$
732 solution model written in Visual Basic for excel. Computers & Geosciences, 28, 597–
733 604.
734 Papale, P., Moretti, R., and Barbato, D. (2006) The compositional dependence of the
735 saturation surface of $H_2O$+$CO_2$ fluids in silicate melts. Chemical Geology, 229, 78–95.
736 Proussevitch, A.A., and Sahagian, D.L. (1998) Dynamics and energetics of bubble growth in
737 magmas: Analytical formulation and numerical modeling. Journal of Geophysical
738 Research, 103, B8, 18223-18251.
739 Proussevitch, A., and Sahagian, D. (2005) Bubbledrive-1: A numerical model of volcanic
740 eruption mechanism driven by disequilibrium magma degassing. Journal of Volcanology
741 and Geothermal Research, 143, 89–111.
742 Prousevitch, A., Sahagian, D., and Anderson, A. (1993) Dynamics of Diffusive Bubble
743 Growth in Magmas: Isothermal Case. Journal of Geophysical Research, 98, B12, 22283–
744 22307.
745 Quane, S.L., Russell, J.K., and Friedlander, E.A. (2009) Time scales of compaction in

volcanic systems. Geology, 37, 471–474.

Redlich, O., and Kwong, J.N.S. (1949) On the Thermodynamics of Solutions. V. An Equation of State. Fugacities of Gaseous Solutions. Chemical Reviews, 44, 233-244.

Robert, G., Russell, J.K., and Giordano, D. (2008) Rheology of porous volcanic materials: High-temperature experimentation under controlled water pressure. Chemical Geology, 256, 216–230.

Russell, J.K., and Quane, S.L. (2005) Rheology of welding: inversion of field constraints. Journal of Volcanology and Geothermal Research, 142, 173–191.

Rust, A.C., and Cashman, K.V. (2007) Multiple origins of obsidian pyroclasts and implications for changes in the dynamics of the 1300 B.P. eruption of Newberry Volcano, USA. Bulletin of Volcanology, 69, 825–845.

Schneider, C.A., Rasband, W.S., and Eliceiri, K.W. (2012) NIH Image to ImageJ: 25 years of image analysis. Nature Methods, 9, 671-675.

Silver, L.A., and Stolper, E. (1989) Water in Albitic Glasses. Journal of Petrology, 30, 667–709.

Silver, L., Ihinger, P., and Stolper, E. (1990) The influence of bulk composition on the speciation of water in silicate glasses. Contributions to Mineralogy and Petrology, 104, 142–162.

Smith, R.L. (1960) Zones and zonal variations in welded ash flows. U.S. Geological Survey Professional Paper 354-F, 10 pp.

Sparks, R.S.J. (1978) The dynamics of bubble formation and growth in magmas: A review and analysis. Journal of Volcanology and Geothermal Research, 3, 1–37.

Sparks, R.S.J., Tait, S.R., and Yanev, Y. (1999) Dense welding caused by volatile resorption. Journal of the Geological Society, London, 156, 217–225.

Stevenson, R.J., Briggs, R.J., and Hodder, A.P.W. (1994) Physical volcanology and

771 emplacement history of the Ben Lomond rhyolite lava flow, Taupo Volcanic Centre,
772 New Zealand. New Zealand Journal of Geology and Geophysics, 37, 345-58.
773 Stevenson, R., Dingwell, D., Bagdassarov, N., and Manley, C. (2001) Measurement and
774 implication of "effective" viscosity for rhyolite flow emplacement. Bulletin of
775 Volcanology, 63, 227–237.
776 Toramaru, A. (1989) Vesiculation Process and Bubble Size Distributions in Ascending
777 Magmas with Constant Velocities. Journal of Geophysical Research, 94, B12, 17523–
778 17542.
779 Toramaru, A. (1995) Numerical study of nucleation and growth of bubbles in viscous
780 magmas. Journal of Geophysical Research, 100, B2, 1913–1931.
781 Tuffen, H., and Castro, J.M. (2009) The emplacement of an obsidian dyke through thin ice:
782 Hrafntinnuhryggur, Krafla Iceland. Journal of Volcanology and Geothermal Research,
783 185, 352–366.
784 Tuffen, H., James, M.R., Castro, J.M., and Schipper, C.I. (2013) Exceptional mobility of an
785 advancing rhyolitic obsidian flow at Cordon Caulle volcano in Chile. Nature
786 Communications, 4, 2709.
787 Vollmayr, K., Kob, W., and Binder, K. (1996) How do the properties of a glass depend on the
788 cooling rate? A computer simulation study of a LennardJones system. Journal of
789 Chemical Physics, 105, 4714-4728.
790 Vona, A., Romano, C., Giordano, D., and Russell, J.K. (2013) The multiphase rheology of
791 magmas from Monte Nuovo (Campi Flegrei, Italy). Chemical Geology, 346, 213–227.
792 Walker, D., and Mullins, O. (1981) Surface Tension of Natural Silicate Melts from 1200-
793 1500$^{o}$C and Implications for Melt Structure. Contributions to Mineralogy and Petrology,
794 76, 455–462.
795 Watkins, J.M., Manga, M., and DePaolo, D.J. (2012) Bubble geobarometry: A record of

pressure changes, degassing, and regassing at Mono Craters, California. Geology, 40, 699–702.

Webster, J.D., and Botcharnikov, R.E. (2011) Distribution of Sulfur Between Melt and Fluid in S-O-H-C-Cl-Bearing Magmatic Systems at Shallow Crustal Pressures and Temperatures. Reviews in Mineralogy & Geochemistry 73, 247-283.

Westrich, H.R., and Eichelberger, J.C. (1994) Gas transport and bubble collapse in rhyolitic magma: an experimental approach. Bulletin of Volcanology, 56, 447-458.

Westrich, H.R., Stockman, H.W., and Eichelberger, J.C. (1988) Degasing of Rhyolitic Magma During Ascent and Emplacement. Journal of Geophysical Research, 93, B6, 6503-6511.

Wright, H.M.N., Cashman, K.V., Rosi, M., and Cioni, R. (2007) Breadcrust bombs as indicators of Vulcanian eruption dynamics at Guagua Pichincha volcano, Ecuador. Bulletin of Volcanology, 69, 281–300.

Yamashita, S. (1999) Experimental Study of the Effect of Temperature on Water Solubility in Natural Rhyolite Melt to 100 MPa. Journal of Petrology, 40, 1497–1507.

Yoshimura, S., and Nakamura, M. (2008) Diffusive dehydration and bubble resorption during open-system degassing of rhyolitic melts. Journal of Volcanology and Geothermal Research, 178, 78–87.

Zhang, Y. (1999) $H_2O$ in rhyolitic glasses and melts: Measurement, speciation, solubility and diffusion. Reviews of Geophysics, 37, 493–516.

Zhang, Y., Xu, Z., Zhu, M., and Wang, H. (2007) Silicate melt properties and volcanic eruptions. Reviews of Geophysics, 45, RG4004.

821 **Figure Captions**

822 **Figure 1.** Images of starting material and experimental run products from the 1000°C suite of
823 experiments. Photographs of (a) the undeformed starting material and experimental run-
824 products (b,c,d). Calculated final porosities and dwell time are listed in the upper left corner
825 of the images. The scale bar at right in photos is marked in mm. X-ray computed tomography
826 (XCT) images from the center of the starting material (e) and the same experimental products
827 (f,g,h). The field of view in each XCT image is 18.2 mm across. The initial heterogeneity in
828 the distributions of bubbles (b,f) is related to cryptic flow banding in the starting material (see
829 text for explanation).
830
831 **Figure 2.** Summary of 1-atmosphere, isothermal, vesiculation experiments. (a) Conceptual
832 diagram of experiments showing a single curve recording volume change as a function of
833 time at fixed *T*. Individual experiments for prescribed dwell times plot as points defining
834 segments of curve: initial state, rapid growth as system expresses its supersaturated state,
835 decreasing growth as system approaches equilibrium, and cessation of exsolution/constant
836 bubble volume at equilibrium. (b) The experimental grid for all experiments plotted as *T* vs. *t*.
837 Each isothermal suite of experiment comprises 3 to 10 runs at different dwell times.
838
839 **Figure 3.** Summary of experimental data from all six suites of isothermal experiments,
840 plotted as porosity ($\phi_f$) vs. time (*t*), including starting material (at *t*=0): (a) 900°C, (b) 925°C,
841 (c) 950°C, (d) 1000°C, (e) 1050°C, (f) 1100°C (cf. Table 2). Each isothermal suite of
842 experiments shows a non-linear increase in porosity with *t* defining a monotonic sharply
843 increasing curve that reaches a final plateau. With increasing *T*, the peak growth rate (*v*')
844 increases (as calculated from the maximum slope of the curve). The final plateau value of
845 $H_2O$ (grey bar) also increases with increasing temperature. For several suites (e.g., 925°C),

the last datum shows a slight relative decrease in porosity, suggesting partial collapse of the sample as the dwell times approach the relaxation timescale of the melt. In all cases analytical uncertainties (1σ) fit within symbols. Also reported are the computed values of viscosity (η; Giordano et al. 2008) and diffusion rate of $H_2O$ (*D*; Zhang et al. 2007) at the experimental temperatures based on the measured $H_2O$ content of 0.11 wt%.

**Figure 4.** Mosaics of color contour images of residual $H_2O$ contents of glassy sample cores measured by FTIR for 1000°C experiments: (a) starting material ($t$=0), (b) $t$=0.5 h, (c) $t$=1.5 h, (d) $t$=2.5 h, (e) $t$=6 h. Final porosity is shown in parentheses. Photos of the glass wafers used for analysis are shown next to each map with a red box showing the analysis location. The color scale bar denotes $H_2O$ content. The starting material is weakly inhomogeneous and shows diffuse banding correlative with slight variations in $H_2O$ content. Experimental products on the other hand show nearly homogeneous distributions of $H_2O$ in the sample, even after only 0.5 h at 1000°C. Circular high or low $H_2O$ content areas are bubbles that either intersect or lie just below the surface of the glass wafer. The high $H_2O$ content rims around these bubbles are artifacts of the imaging around the edge of the bubble (see text for explanation). All scale bars are 350 μm for FTIR contour maps, and 5 mm for photos of glass wafers.

**Figure 5.** Volume and $H_2O$ content changes in each sample during experiments. (a) Observed changes in sample volume ($\Delta V/V_i$) plotted against experimental $T$ (°C) for all experiments (Table 2). The isothermal experiments show an increase in $\Delta V/V_i$ with increasing experimental dwell time (arrow at right). Samples below the equilibrium plateau part of the curve (cf. Fig. 2a; Fig. 3) are open symbols; equilibrium plateau samples are closed. (b) The calculated $H_2O$ contents (wt%) of the residual glass in each sample vs. $T$ (°C) for all

871 experiments (Table 3). Residual $H_2O$ contents of the glass decrease with increasing dwell
872 time within each isothermal set of experiments and with increasing *T*. Symbols as in (a).
873
874 **Figure 6.** Residual $H_2O$ contents as mole fraction ($X_{H2O}$) and experimental temperature. (a)
875 Calculated values of ln $X_{H2O}$ vs. 1000/*T* (K). Closed symbols denote plateau samples. The
876 linear best-fit line for 900-1050°C plateau samples is shown as a solid black line. Thick grey
877 line is measured $H_2O$ content of starting material. (b) The residual $H_2O$ contents as ln $X_{H2O}$
878 vs. 1000/*T* (K) for the plateau samples from this study (closed circles) as well as all published
879 0.1 MPa rhyolitic data (Appendix A), including Liu et al. (2005) (open circles), Friedman et
880 al. (1963) (open triangles) and McMillan et al. (1986) (open square). Broken lines show
881 published models (500-1250°C). Solid line is our linear best-fit. The models of Moore et al.
882 (1998) and Papale et al. (2006) plot off the scale at lower $H_2O$ contents. Our best-fit model
883 agrees well the data from Liu et al. (2005), as well as with the Liu et al. (2005), Zhang et al.
884 (2007) and Newman and Lowenstern (2002) $H_2O$ solubility models. All models fail to
885 capture all the Friedman et al. (1963) and McMillan et al. (1986) data.
886
887 **Figure 7.** Isobaric $H_2O$ solubility curves (grey lines) predicted by Liu et al. (2005) model and
888 plotted as *T* (°C) vs. $H_2O$ content (wt%) for a range of P (numbers on lines, in MPa). Our
889 model is the thick black line at 0.1 MPa. Thin solid black curve is glass transition
890 temperature (*Tg* (°C)) of the rhyolite melt with increasing $H_2O$ content (Giordano et al.
891 2008). The intersection of the *Tg* curve with the isobars marks the maximum possible $H_2O$
892 content of the melt at a given pressure. Here, the drop in *Tg* with increasing $H_2O$ content is
893 insufficient to accommodate further $H_2O$ resorption, thereby, causing a 'rehydration quench'
894 of the melt to a glass.
895

**Figure 8**. Model isobaric (0.01 - 20 MPa) rehydration-cooling paths in volcanic systems and corresponding glass transition temperatures (*Tg*). Inset shows diverse paths for volcanic systems to intersect their *Tg*'s, including: i) cooling at rates faster than the melt changes composition ('thermal quench', A), ii) cooling paths allowing for $H_2O$ resorption and reducing melt *Tg* ('rehydration quench', B), and iii) exsolution and loss of $H_2O$ causing a rise in melt *Tg* ('degassing quench', C). Schematic arrows in main figure show simplified volcanic processes including: isobaric thermal quench (A), rehydration quench ($B_1$) and degassing quench (C) at elevated pressure; isothermal eruption (arrow labeled 'pyroclastic fallout') followed by cooling and rehydration ($B_2$); and isothermal accumulation (arrow labeled 'ignimbrite') promoting isobaric cooling and rehydration ($B_3$). The grey arrows show the variations in $H_2O$ content and *Tg* depending on the external pressure and cooling rate of different volcanic processes (see text for explanation).

**Figure 9.** Coupled effects of retrograde solubility and 'rehydration quench' in surficial deposits and within volcanic conduits. (a) Solid grey line represents the isothermal (800°C) *P*-dependence of $H_2O$ solubility (e.g., Sparks et al., 1999). The increase in load pressure allows for increased $H_2O$ solubility but does not include the effects of retrograde solubility in a cooling melt (arrow) leading to underestimation of final $H_2O$ contents. (b) Differences in $H_2O$ contents (wt%); black lines) and *Tg* values normalized to their anhydrous values (grey lines) as a function of P for an isothermal melt (800°C melt; dashed lines) vs. a cooling melt (solid lines) for a 100 m thick ignimbrite sheet or lava. The difference in curves shows the effects of 'rehydration quenching' on $H_2O$ contents and *Tg* of the melt. Over 100 m $H_2O$ resorption in the cooling melt increases the $H_2O$ content by ~0.1 wt% and depresses *Tg* by 15°C relative to an isothermal melt. (c) The difference between $H_2O$ content and *Tg* in an isothermal (800°C) versus a cooling melt in the context of the upper conduit (2000 m). Lines

as in (b). Over 2000 m there is a ~1.0 wt% increase in $H_2O$ content and a ~50°C decrease in *Tg* in a cooling melt relative to an isothermal one.

**Table 1**. Major anhydrous element composition of obsidian from Hrafntinnuhryggur, Krafla, Iceland.

| | S11b[a] | UBC-Std4[b] |
|---|---|---|
| Method | EMPA | XRF |
| $SiO_2$ | 75.23 | 74.77 |
| $TiO_2$ | 0.23 | 0.23 |
| $Al_2O_3$ | 12.00 | 12.31 |
| $Fe_2O_3$ | - | 0.69 |
| FeO | 3.28 | 2.48 |
| MnO | 0.11 | 0.11 |
| MgO | 0.10 | 0.14 |
| CaO | 1.66 | 1.64 |
| $Na_2O$ | 4.15 | 4.28 |
| $K_2O$ | 2.75 | 2.60 |
| $P_2O_5$ | - | 0.03 |
| Total | 99.51 | 99.28 |
| $FeO_T$ | 3.28 | 3.10 |

[a]Electron microprobe analysis of glass (Tuffen and Castro, 2009).

[b]Bulk XRF analysis of glass by ALS-Chemex.

**Table 2**. Experimental conditions and properties of all pre- and post-experiment cores including: time (t), initial and final mass (m), final density ($\rho_f$), volume change ($\Delta V$) and final porosity ($\phi_f$)

| LABEL | $T_{exp}$ (°C) | t (h) | $m_i$ (g) | $m_f$ (g) | $\rho_f$ (g cm$^{-3}$)[a] | $\Delta V$ (cm$^3$) | $\phi_f$ (%)[b] |
|---|---|---|---|---|---|---|---|
| AR-IK-28 | 0 | 0 | 1.702 | 1.702 | 2.394 | 0 | 0 |
| AR-IK-39 | 900 | 5.0 | 1.600 | 1.600 | 2.372 | 0.02 | 3.07 |
| AR-IK-40 | 900 | 7.5 | 1.575 | 1.575 | 2.056 | 0.12 | 15.15 |
| AR-IK-46 | 900 | 9.0 | 1.571 | 1.570 | 2.053 | 0.12 | 15.10 |
| AR-IK-54 | 900 | 12.3 | 1.824 | 1.824 | 1.856 | 0.23 | 23.34 |
| AR-IK-49 | 900 | 13.0 | 1.953 | 1.952 | 2.105 | 0.11 | 11.56 |
| AR-IK-52 | 900 | 16.8 | 2.210 | 2.209 | 1.807 | 0.30 | 24.66 |
| AR-IK-24 | 900 | 20.0 | 1.639 | 1.637 | 1.344 | 0.53 | 43.25 |
| AR-IK-50 | 900 | 24.0 | 1.764 | 1.763 | 1.340 | 0.56 | 42.77 |
| AR-IK-44 | 925 | 2.5 | 1.676 | 1.676 | 2.313 | 0.03 | 4.24 |
| AR-IK-42 | 925 | 5.0 | 1.732 | 1.731 | 1.797 | 0.25 | 25.71 |
| AR-IK-43 | 925 | 12.0 | 1.713 | 1.712 | 1.462 | 0.47 | 39.74 |
| AR-IK-45 | 925 | 20.0 | 1.827 | 1.826 | 1.188 | 0.78 | 50.60 |
| AR-IK-51 | 925 | 24.0 | 1.612 | 1.611 | 1.415 | 0.46 | 40.24 |
| AR-IK-10 | 950 | 1.5 | 1.720 | 1.719 | 1.916 | 0.16 | 18.25 |
| AR-IK-7 | 950 | 4.0 | 1.676 | 1.675 | 1.215 | 0.67 | 48.83 |
| AR-IK-48 | 950 | 6.0 | 1.654 | 1.653 | 1.131 | 0.78 | 53.36 |
| AR-IK-11 | 950 | 12.5 | 1.648 | 1.647 | 1.007 | 0.94 | 57.41 |
| AR-IK-25 | 950 | 20.0 | 1.872 | 1.871 | 1.100 | 0.92 | 53.87 |
| AR-IK-21 | 1000 | 0.5 | 1.675 | 1.675 | 1.901 | 0.19 | 21.23 |
| AR-IK-17 | 1000 | 1.5 | 1.617 | 1.617 | 1.275 | 0.59 | 46.54 |
| AR-IK-22 | 1000 | 1.5 | 1.819 | 1.817 | 1.109 | 0.88 | 53.71 |
| AR-IK-16 | 1000 | 2.5 | 1.632 | 1.630 | 0.796 | 1.37 | 66.69 |
| glass 4 | 1000 | 4.0 | 2.324 | 2.322 | 0.895 | 1.58 | 60.74 |
| AR-IK-12 | 1000 | 4.0 | 1.716 | 1.714 | 0.906 | 1.17 | 61.64 |
| AR-IK-20 | 1000 | 4.0 | 1.714 | 1.713 | 0.888 | 1.22 | 63.05 |
| AR-IK-34 | 1000 | 4.0 | 1.728 | 1.726 | 0.799 | 1.43 | 66.40 |
| AR-IK-18 | 1000 | 7.5 | 1.531 | 1.529 | 0.822 | 1.22 | 65.80 |
| AR-IK-27 | 1000 | 13.0 | 1.884 | 1.883 | 0.936 | 1.22 | 60.87 |
| AR-IK-32 | 1050 | 0.5 | 1.736 | 1.736 | 1.950 | 0.17 | 18.80 |
| AR-IK-33 | 1050 | 1.2 | 1.734 | 1.733 | 1.008 | 1.00 | 58.17 |
| AR-IK-47 | 1050 | 3.0 | 1.680 | 1.679 | 0.843 | 1.30 | 65.22 |
| AR-IK-23 | 1050 | 4.0 | 1.701 | 1.699 | 0.712 | 1.68 | 70.42 |
| AR-IK-35 | 1050 | 5.0 | 1.726 | 1.724 | 0.759 | 1.54 | 68.00 |
| AR-IK-30 | 1100 | 0.5 | 1.731 | 1.730 | 1.115 | 0.85 | 54.92 |
| AR-IK-31 | 1100 | 1.0 | 1.730 | 1.728 | 0.696 | 1.78 | 71.60 |
| AR-IK-36 | 1100 | 2.0 | 1.725 | 1.723 | 0.762 | 1.54 | 67.91 |

[a]Mean density (2.394 g cm$^{-3}$) is based on an initial porosity below detection.

[b] $\phi_f = 100\ \Delta V/V_f$, where $V_f$ is the final volume.

**Table 3**. Model values of residual $H_2O$ in glasses from 1 atm isothermal vesiculation experiments. We assume an initial $H_2O$ content of 0.114 wt. %[a], constant surface tension (0.081 N $m^{-1}$), and an average mean bubble radius of 0.322 mm for an internal pressure of 101828 Pa[b]. Residual $H_2O$ is calculated from sample volume change (ΔV) using the Redlich-Kwong equation of state (see text for full explanation).

| | Measured Properties | | | | Calculated Properties | | | | |
|---|---|---|---|---|---|---|---|---|---|
| Sample | $H_2O$[c] | $m_i$[d] | ΔV ($m^3$) | $_f$ (%)[e] | $n_i$[f] | $n_b$[g] | $n_r$[h] | $H_2O_{gf}$ | $\Delta H_2O$[i] |
| AR-IK-28 | 0.114 | 1.702 | 0 | 0 | 1.08E-04 | - | - | 0.114 | |
| AR-IK-39 | | 1.600 | 2.07E-08 | 3.07 | 1.01E-04 | 2.16E-07 | 1.01E-04 | 0.114 | |
| AR-IK-40 | | 1.575 | 1.16E-07 | 15.15 | 9.97E-05 | 1.21E-06 | 9.85E-05 | 0.113 | |
| AR-IK-46 | | 1.571 | 1.16E-07 | 15.10 | 9.94E-05 | 1.21E-06 | 9.82E-05 | 0.113 | |
| AR-IK-54 | | 1.824 | 2.29E-07 | 23.34 | 1.15E-04 | 2.39E-06 | 1.13E-04 | 0.112 | |
| AR-IK-49 | | 1.953 | 1.07E-07 | 11.56 | 1.24E-04 | 1.12E-06 | 1.22E-04 | 0.113 | |
| AR-IK-52 | | 2.210 | 3.01E-07 | 24.66 | 1.40E-04 | 3.15E-06 | 1.37E-04 | 0.111 | |
| AR-IK-24 | 0.098 | 1.639 | 5.27E-07 | 43.25 | 1.04E-04 | 5.50E-06 | 9.82E-05 | 0.108 | -0.010 |
| AR-IK-50 | | 1.764 | 5.63E-07 | 42.77 | 1.12E-04 | 5.88E-06 | 1.06E-04 | 0.108 | |
| AR-IK-44 | | 1.676 | 3.07E-08 | 4.24 | 1.06E-04 | 3.14E-07 | 1.06E-04 | 0.114 | |
| AR-IK-42 | | 1.732 | 2.48E-07 | 25.71 | 1.10E-04 | 2.53E-06 | 1.07E-04 | 0.111 | |
| AR-IK-43 | | 1.713 | 4.65E-07 | 39.74 | 1.08E-04 | 4.76E-06 | 1.04E-04 | 0.109 | |
| AR-IK-45 | | 1.827 | 7.78E-07 | 50.60 | 1.16E-04 | 7.96E-06 | 1.08E-04 | 0.106 | |
| AR-IK-51 | | 1.612 | 4.58E-07 | 40.24 | 1.02E-04 | 4.68E-06 | 9.73E-05 | 0.109 | |
| AR-IK-10 | | 1.720 | 1.64E-07 | 18.25 | 1.09E-04 | 1.64E-06 | 1.07E-04 | 0.112 | |
| AR-IK-7 | | 1.676 | 6.73E-07 | 48.83 | 1.06E-04 | 6.74E-06 | 9.93E-05 | 0.107 | |
| AR-IK-48 | | 1.654 | 7.79E-07 | 53.36 | 1.05E-04 | 7.80E-06 | 9.69E-05 | 0.106 | |
| AR-IK-11 | | 1.648 | 9.39E-07 | 57.41 | 1.04E-04 | 9.40E-06 | 9.49E-05 | 0.104 | |
| AR-IK-25 | 0.087 | 1.872 | 9.16E-07 | 53.87 | 1.18E-04 | 9.17E-06 | 1.09E-04 | 0.105 | -0.018 |
| AR-IK-21 | | 1.675 | 1.87E-07 | 21.23 | 1.06E-04 | 1.80E-06 | 1.04E-04 | 0.112 | |
| AR-IK-17 | | 1.617 | 5.90E-07 | 46.54 | 1.02E-04 | 5.68E-06 | 9.67E-05 | 0.108 | |
| AR-IK-22 | | 1.819 | 8.80E-07 | 53.71 | 1.15E-04 | 8.47E-06 | 1.07E-04 | 0.106 | |
| AR-IK-16 | | 1.632 | 1.37E-06 | 66.69 | 1.03E-04 | 1.31E-05 | 9.02E-05 | 0.099 | |
| glass 4 | | 2.324 | 1.58E-06 | 60.74 | 1.47E-04 | 1.52E-05 | 1.32E-04 | 0.102 | |
| AR-IK-12 | | 1.716 | 1.17E-06 | 61.64 | 1.09E-04 | 1.12E-05 | 9.73E-05 | 0.102 | |
| AR-IK-20 | | 1.714 | 1.22E-06 | 63.05 | 1.08E-04 | 1.17E-05 | 9.68E-05 | 0.102 | |
| AR-IK-34 | | 1.728 | 1.43E-06 | 66.40 | 1.09E-04 | 1.38E-05 | 9.55E-05 | 0.100 | |
| AR-IK-18 | 0.093 | 1.531 | 1.22E-06 | 65.80 | 9.69E-05 | 1.18E-05 | 8.51E-05 | 0.100 | -0.007 |

| | | | | | | | | | |
|---|---|---|---|---|---|---|---|---|---|
| AR-IK-27 | | 1.884 | 1.22E-06 | 60.87 | 1.19E-04 | 1.18E-05 | 1.07E-04 | 0.103 | |
| AR-IK-32 | | 1.736 | 1.67E-07 | 18.80 | 1.10E-04 | 1.55E-06 | 1.08E-04 | 0.112 | |
| AR-IK-33 | | 1.734 | 1.00E-06 | 58.17 | 1.10E-04 | 9.26E-06 | 1.00E-04 | 0.104 | |
| AR-IK-47 | | 1.680 | 1.30E-06 | 65.22 | 1.06E-04 | 1.20E-05 | 9.43E-05 | 0.101 | |
| AR-IK-23 | 0.090 | 1.701 | 1.68E-06 | 70.42 | 1.08E-04 | 1.56E-05 | 9.21E-05 | 0.098 | -0.007 |
| AR-IK-35 | | 1.726 | 1.54E-06 | 68.00 | 1.09E-04 | 1.43E-05 | 9.49E-05 | 0.099 | |
| AR-IK-30 | | 1.731 | 8.52E-07 | 54.92 | 1.10E-04 | 7.60E-06 | 1.02E-04 | 0.106 | |
| AR-IK-31 | 0.108 | 1.730 | 1.78E-06 | 71.60 | 1.09E-04 | 1.59E-05 | 9.36E-05 | 0.097 | 0.010 |
| AR-IK-36 | | 1.725 | 1.54E-06 | 67.91 | 1.09E-04 | 1.37E-05 | 9.54E-05 | 0.100 | |

[a]Initial water content is based on FTIR anaysis. [b]Calculated internal pressure (Pa) [$P_i=P_e+2\sigma\ r^{-1}$].
[c]Measured $H_2O$ content (wt%) in cores by FTIR. [d]Initial mass (g) of sample core. [e]Porosity of sample based on volume change. [f,g,h]Calculated moles of $H_2O$ dissolved in initial sample, exsolved as bubbles and remaining in sample, respectively. [i]Measured - calculated $H_2O$ content of glass run products.

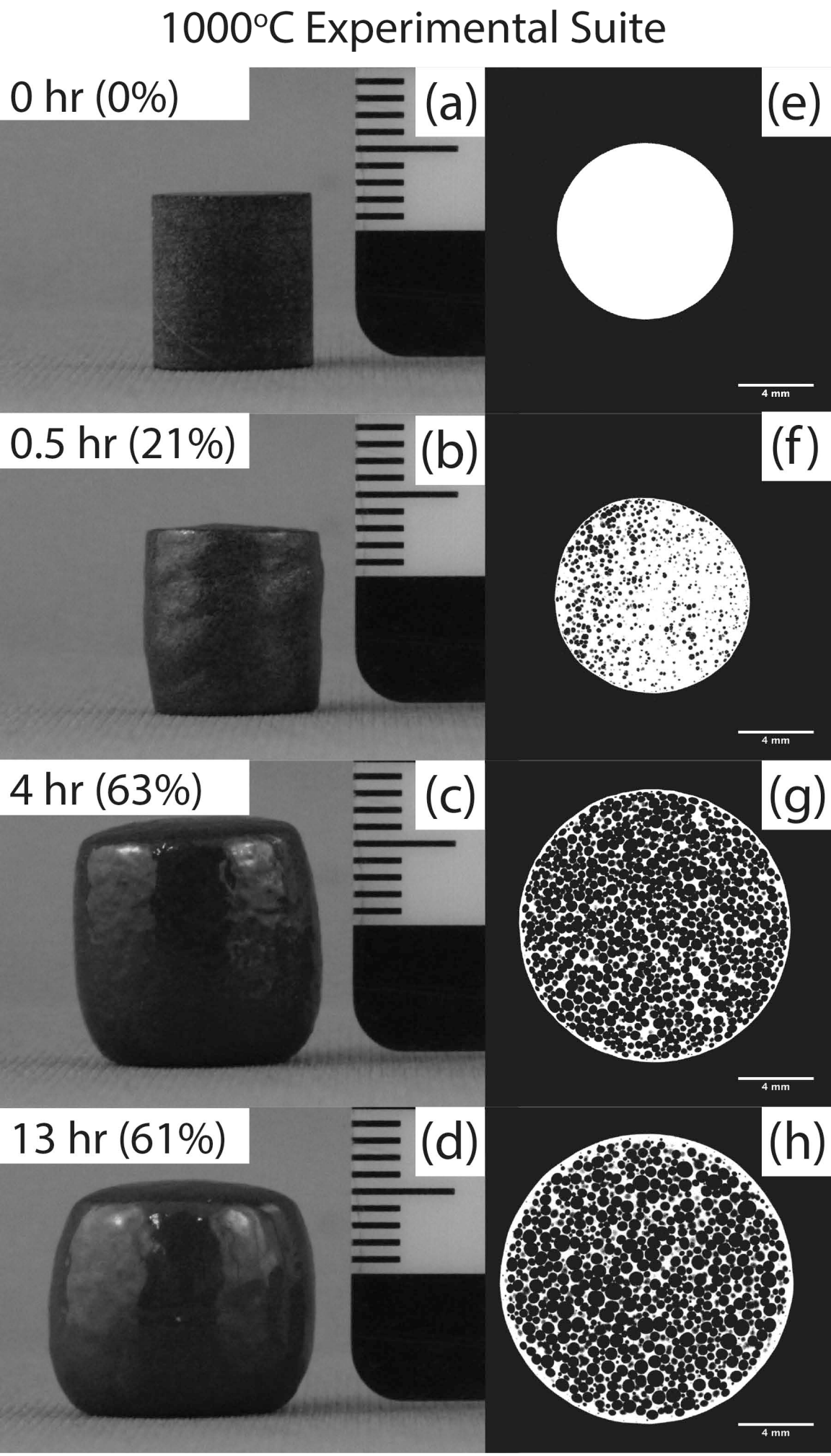


Ryan et al. (2014) FIGURE 1

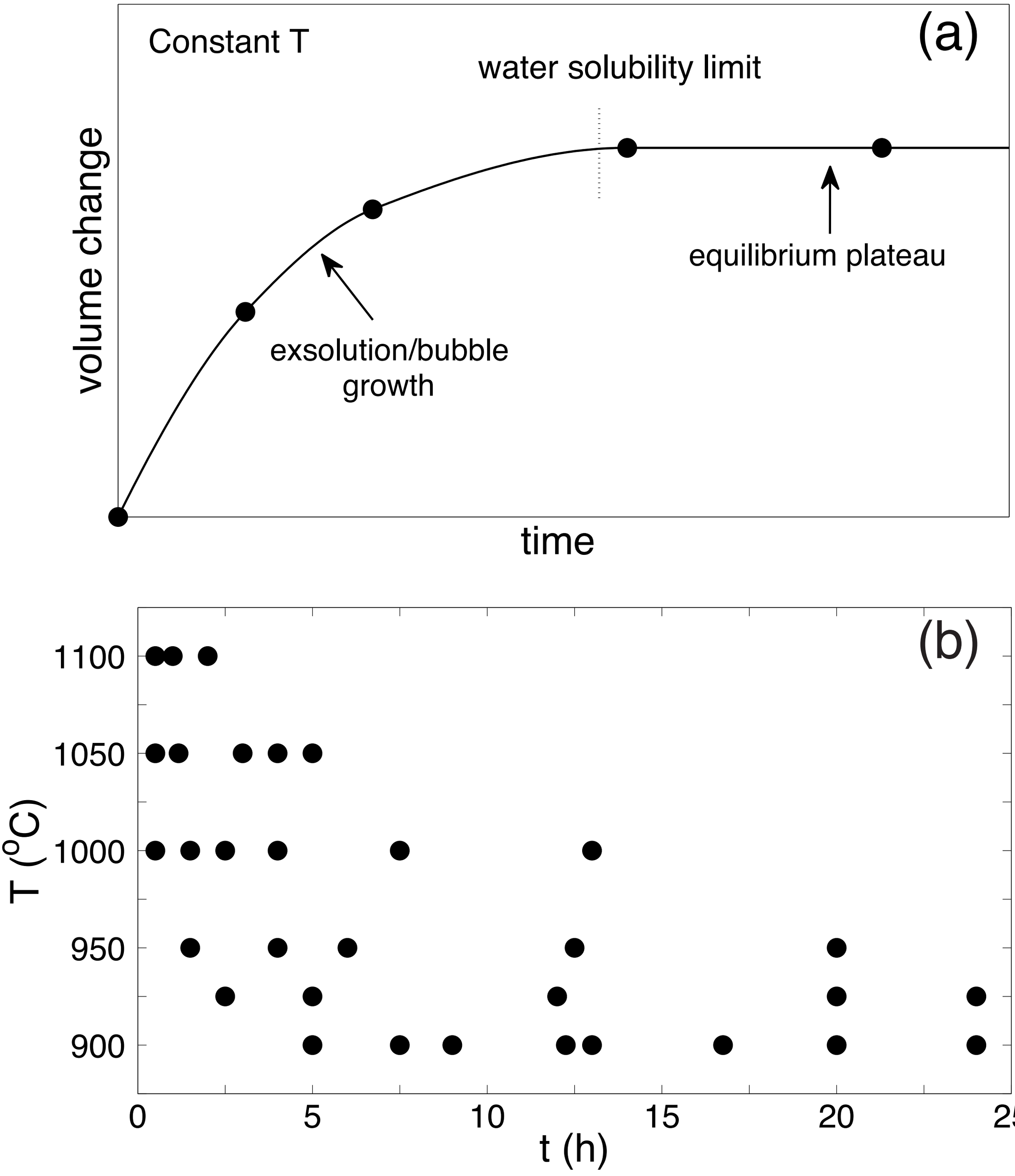


Ryan et al. (2014) FIGURE 2

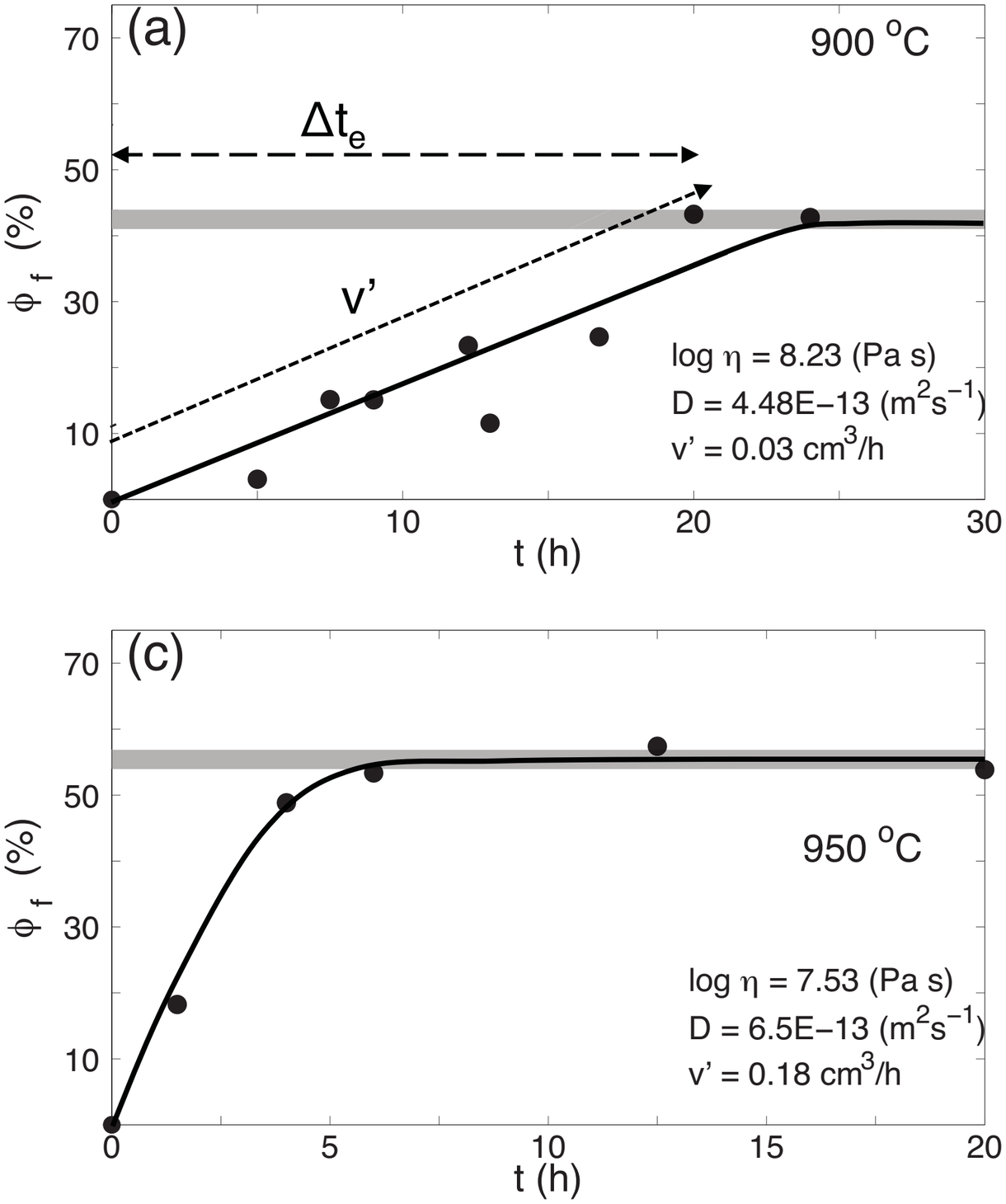


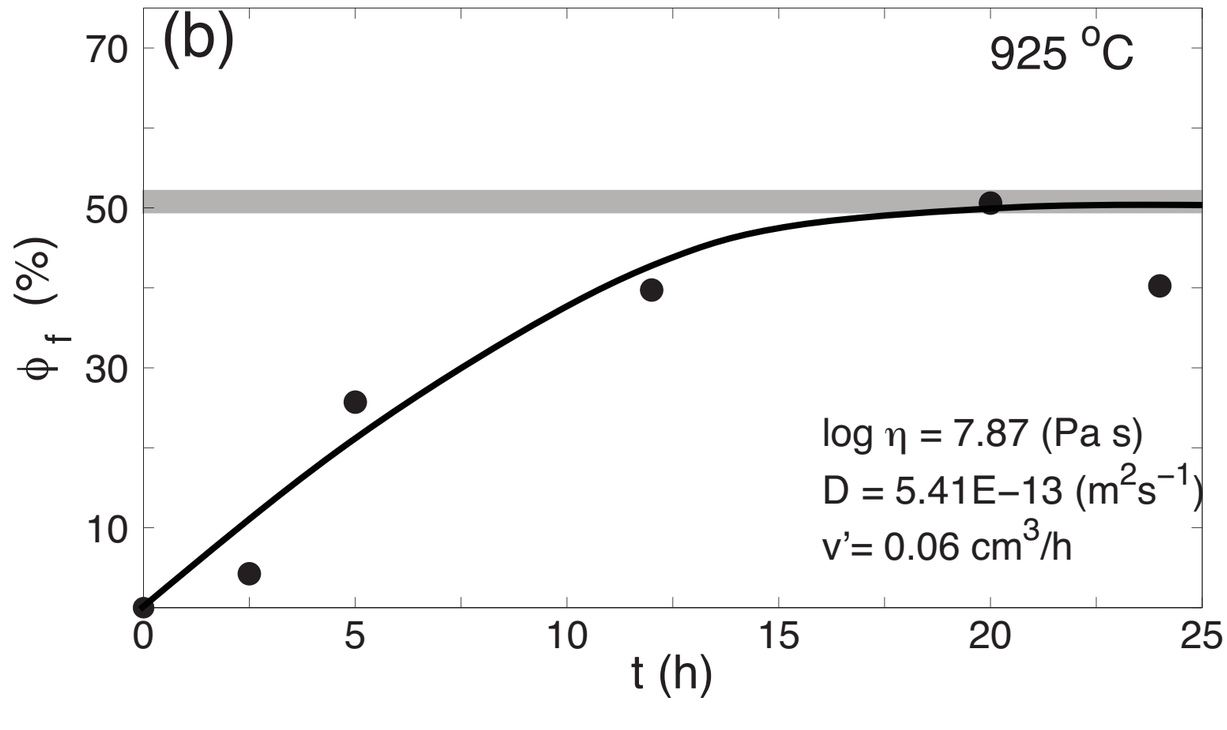





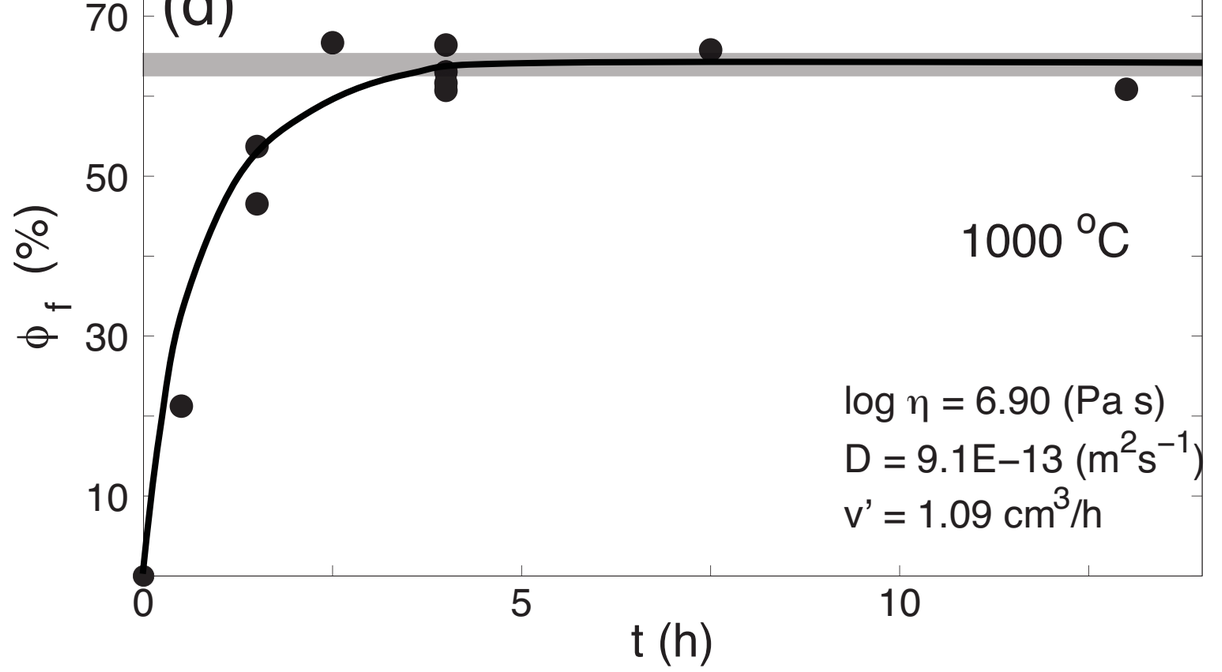


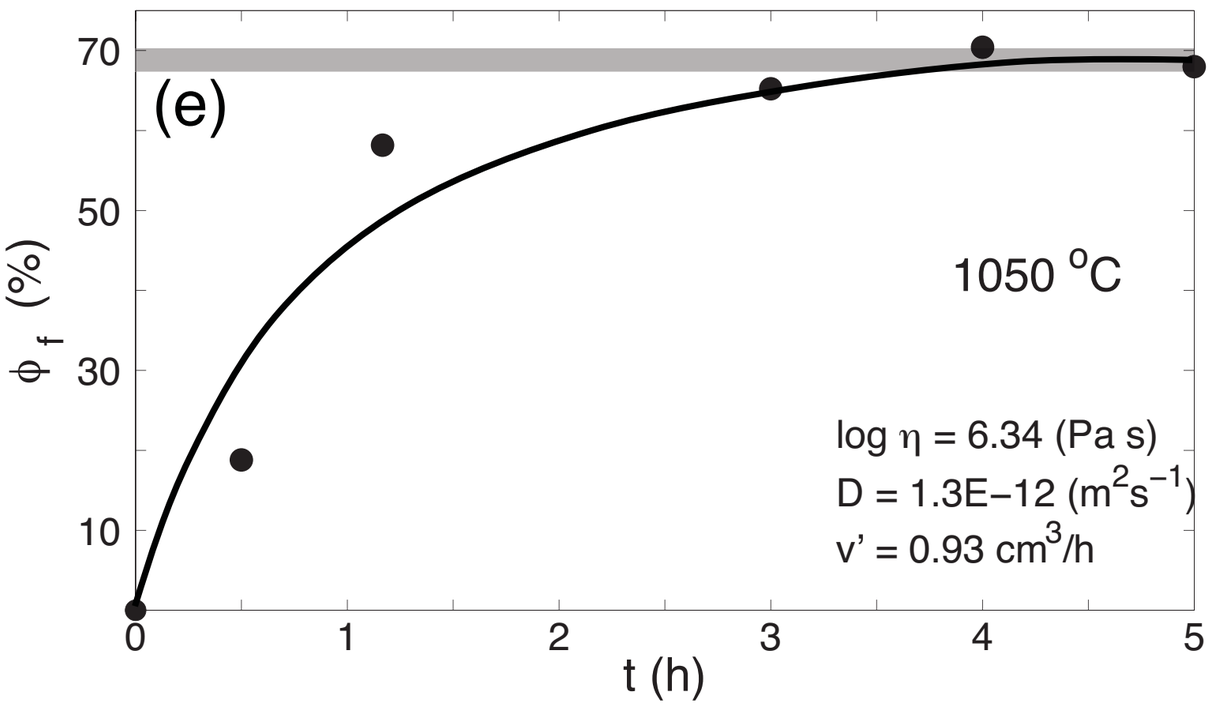


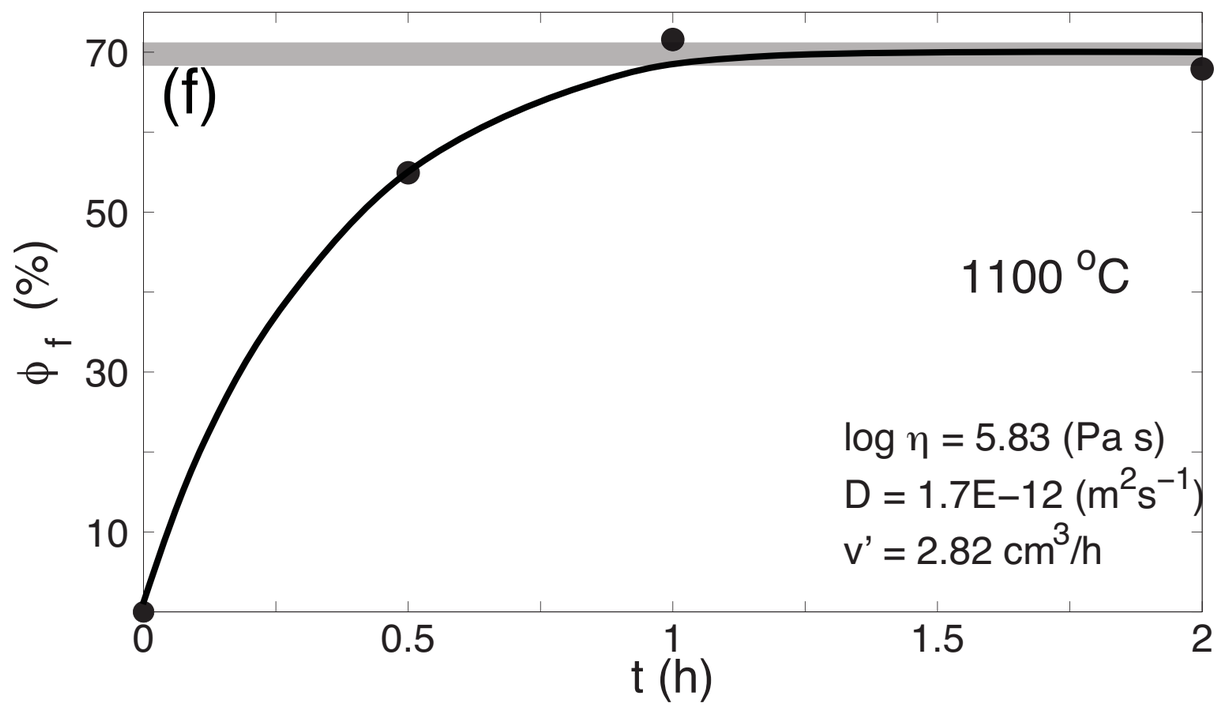


Ryan et al. (2014) FIGURE 3

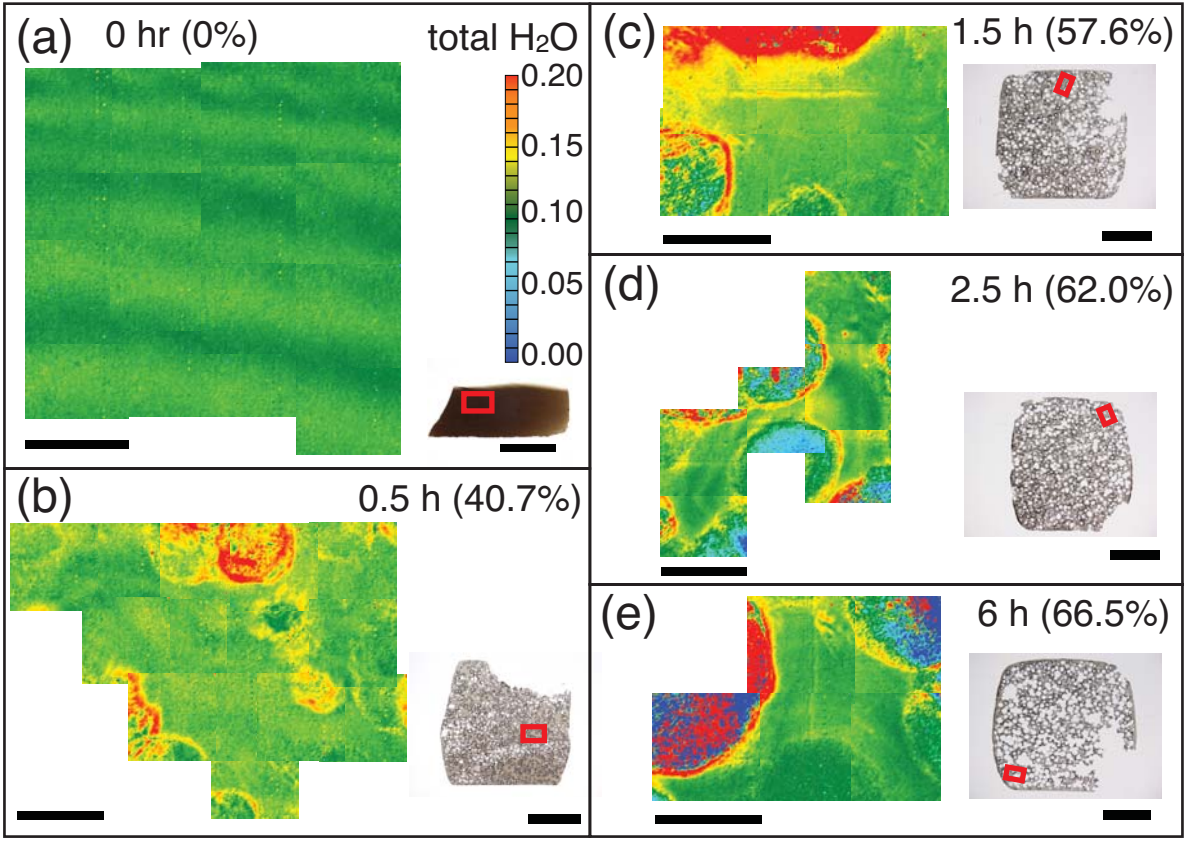


Ryan et al. (2014) FIGURE 4

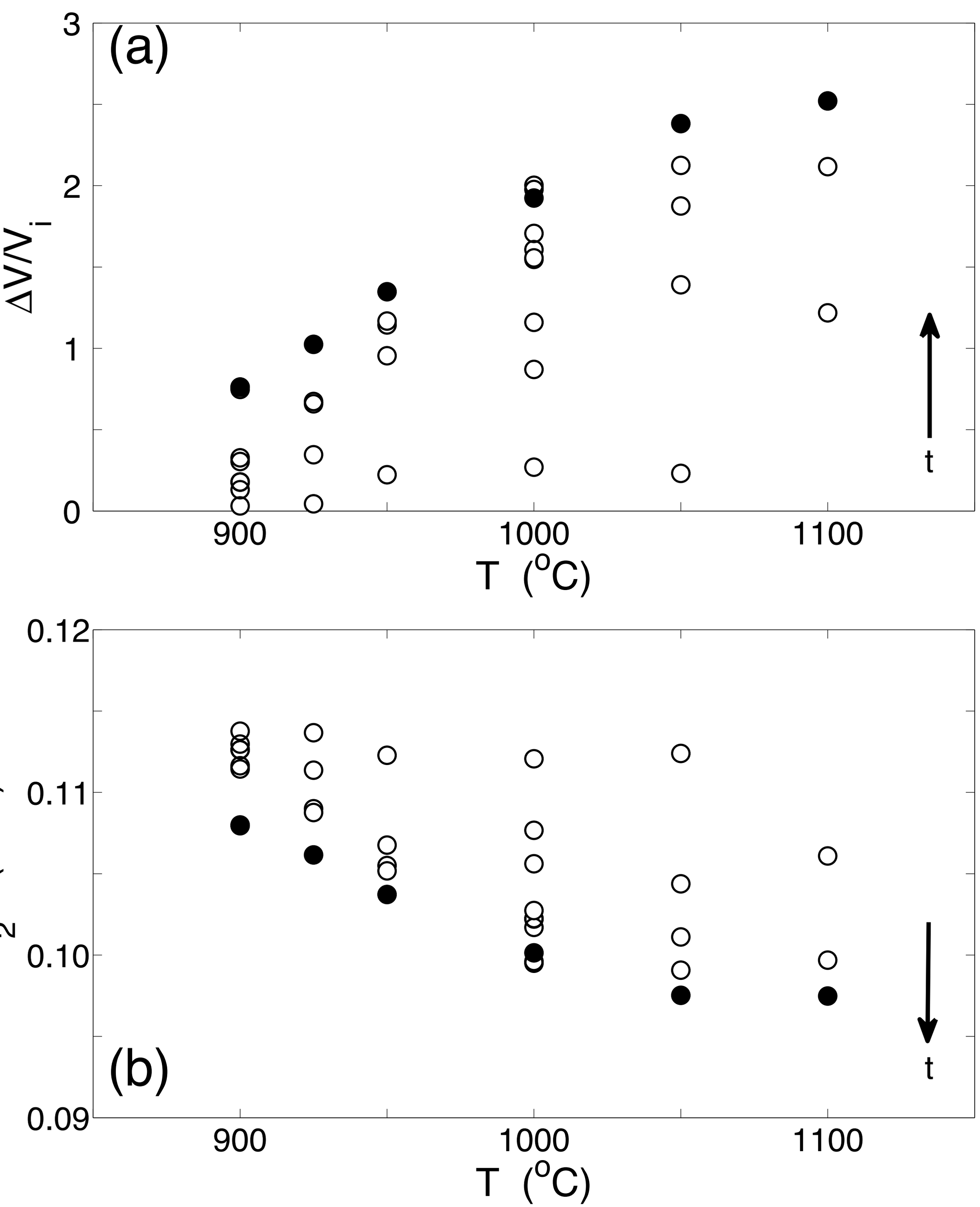


Ryan et al. (2014) FIGURE 5

1100°C
900°C
(a)
−5.45
−5.55
−5.65
$\ln(X_{H_2O})$
0.72
0.76
0.80
0.84
1000/T (K)
1250°C
500°C
(b)
−4.5
−5
−5.5
−6
−6.5
−7
−7.5
$\ln(X_{H_2O})$
0.7
0.8
0.9
1.0
1.1
1.2
1.3
1000/T (K)
Liu et al. (2005)
Zhang et al. (2007)
Newman and Lowenstern (2002)
linear best–fit

Ryan et al. (2014) FIGURE 6

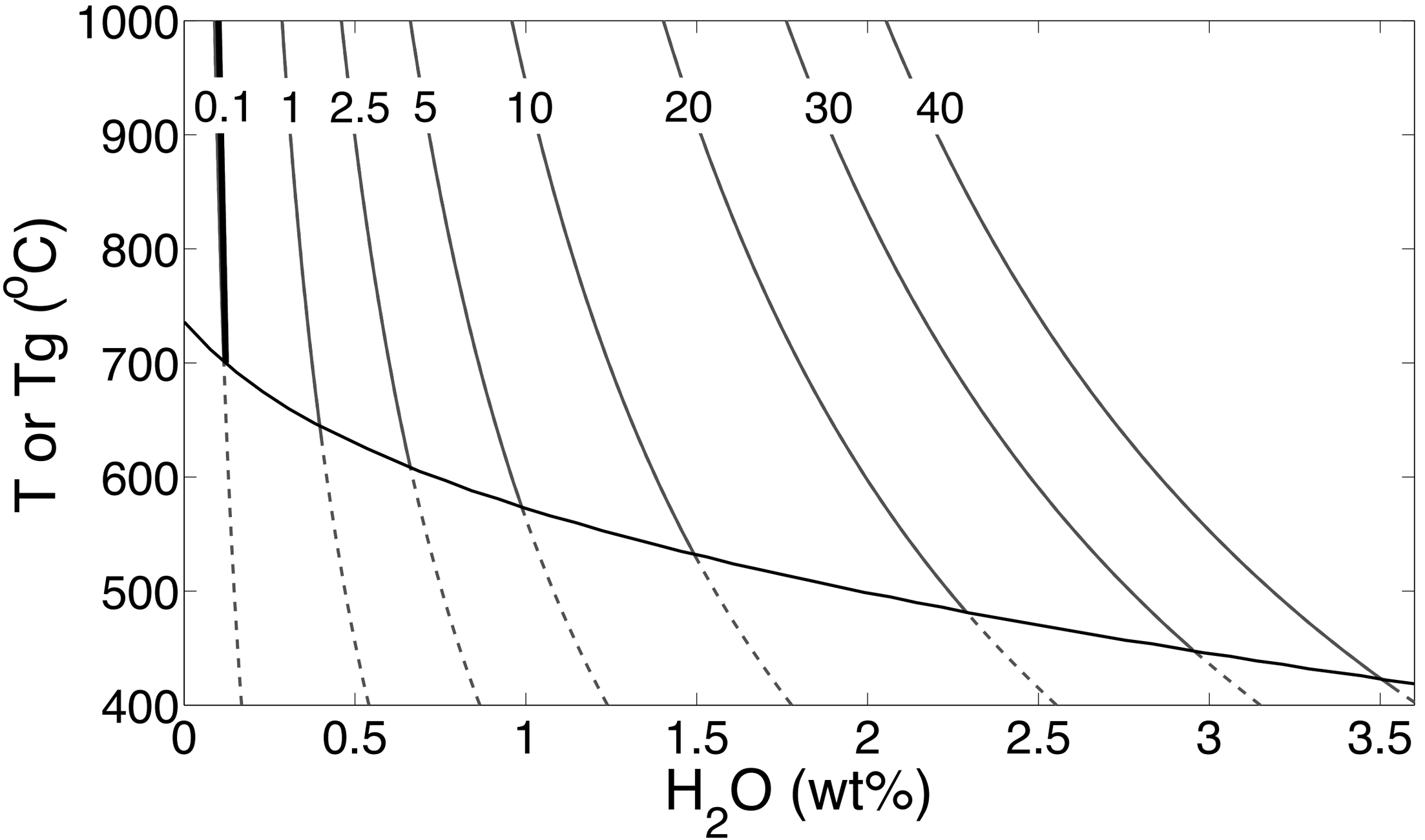


Ryan et al. (2014) FIGURE 7

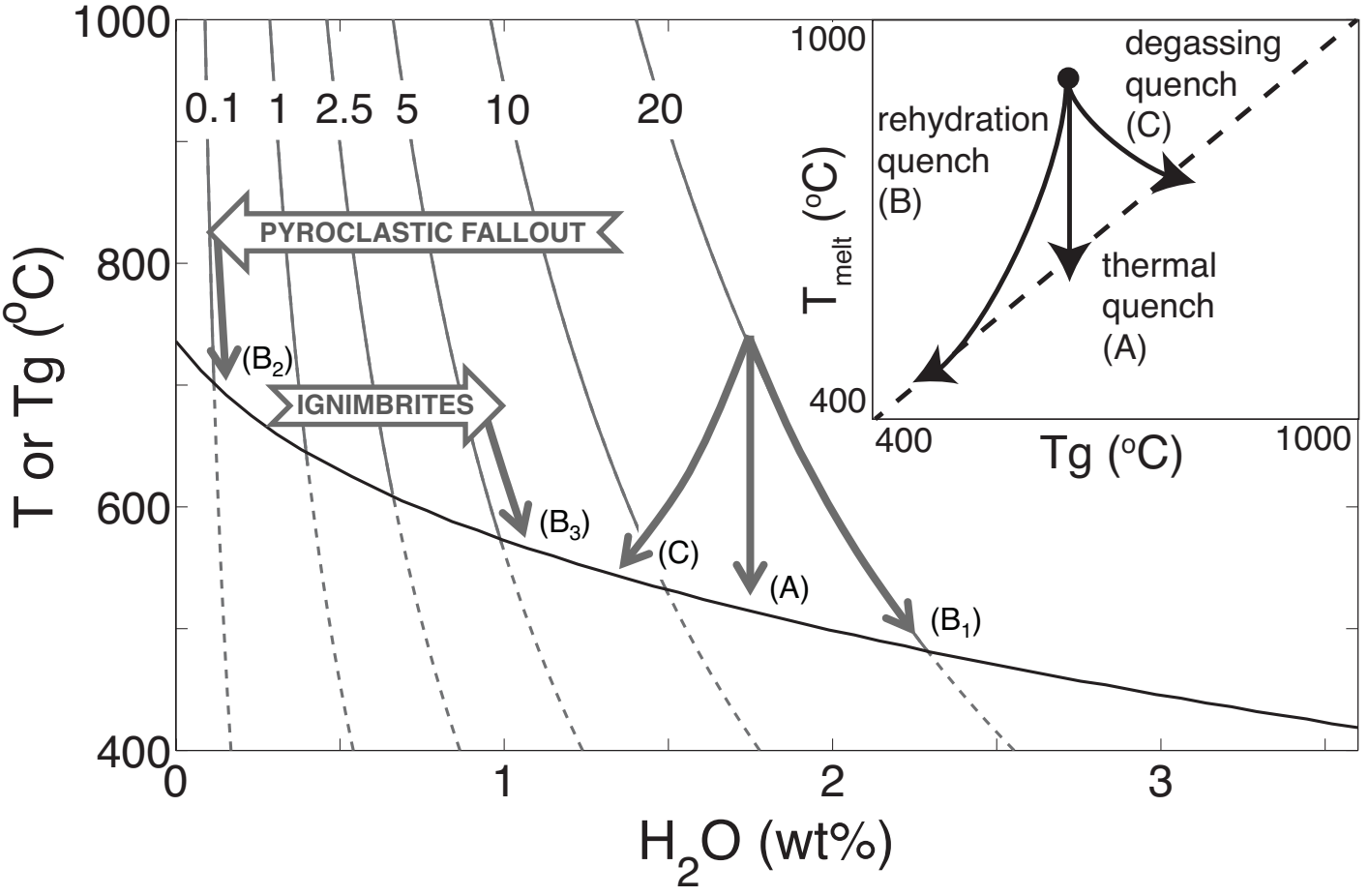


Ryan et al. (2014) FIGURE 8

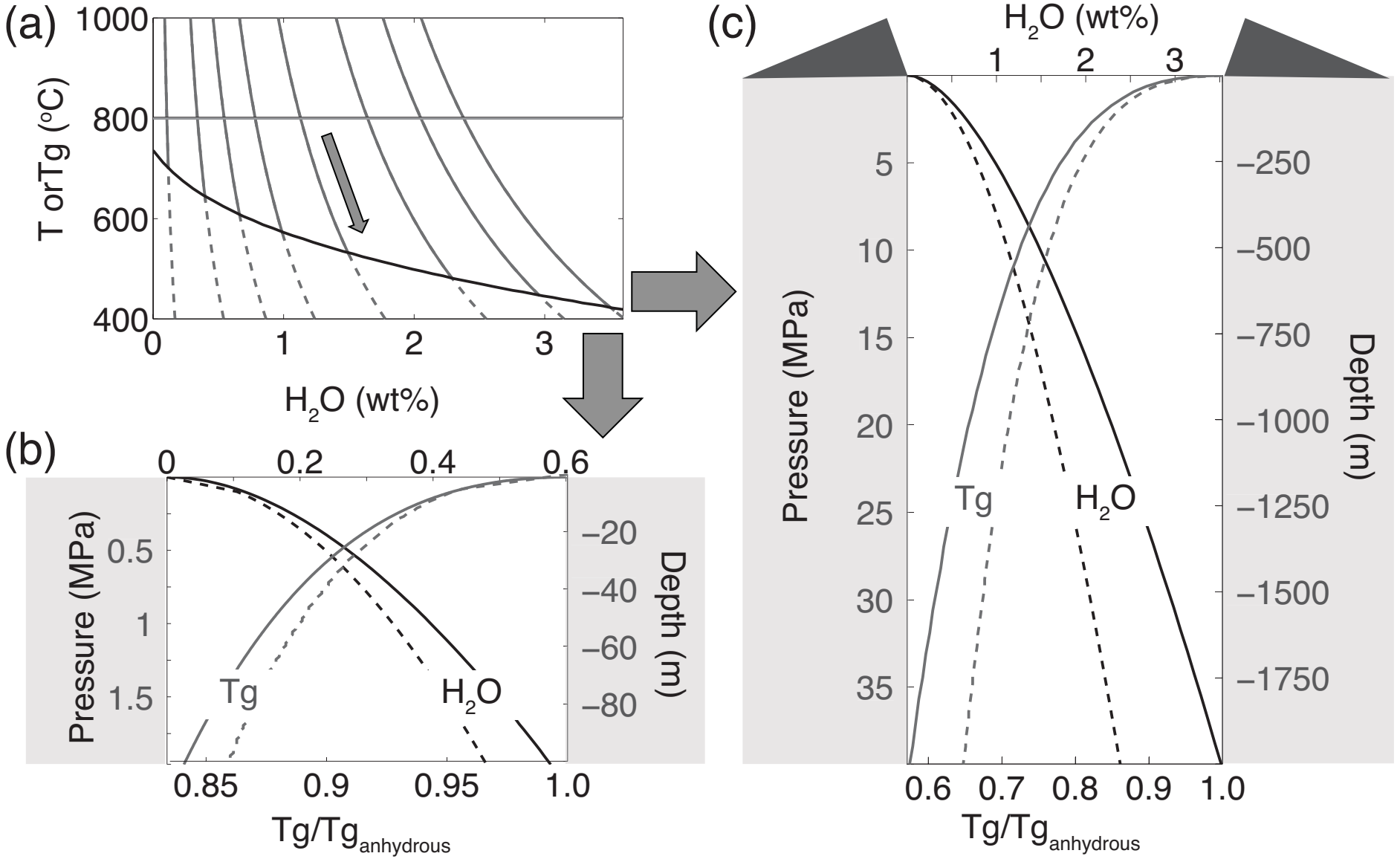


Ryan et al. (2014) FIGURE 9